# Drag Minimization Based on the Navier-Stokes Equations Using a Newton-Krylov Approach

Lana Osusky[1], Howard Buckley [2], Thomas Reist [3], and David W. Zingg[4]
*University of Toronto, Toronto, Ontario, M3H 5T6, Canada*

**A methodology is presented for performing numerical aerodynamic shape optimization based on the three-dimensional Reynolds-averaged Navier-Stokes (RANS) equations. An initial multi-block structured mesh is first fit with B-spline volumes which form the basis for a hybrid mesh movement scheme that is tightly integrated with the geometry parameterization based on B-spline surfaces. The RANS equations and the one-equation Spalart-Allmaras turbulence model are solved in a fully coupled manner using an efficient parallel Newton-Krylov algorithm with approximate-Schur preconditioning. Gradient evaluations are performed using the discrete-adjoint approach with analytical differentiation of the discrete flow and mesh movement equations. The overall methodology remains robust even in the presence of large shape changes. Several examples of lift-constrained drag minimization are provided, including a study of the Common Research Model (CRM) wing geometry, a wing-body-tail geometry with a prescribed spanwise load distribution, and a Blended-Wing-Body (BWB) configuration. An example is provided that demonstrates that a wing optimized based on the Euler equations exhibits substantially inferior performance when subsequently analyzed based on the RANS equations relative to a wing optimized based on the RANS equations.**

---

[1] Member AIAA (currently Mechanical Engineer, GE Global Research)
[2] Research Associate, University of Toronto Institute for Aerospace Studies
[3] Ph.D. Candidate, University of Toronto Institute for Aerospace Studies
[4] Professor and Director, Tier 1 Canada Research Chair in Computational Fluid Dynamics and Environmentally Friendly Aircraft Design, J. Armand Bombardier Foundation Chair in Aerospace Flight, AIAA Associate Fellow.

**Nomenclature**

| | |
|---|---|
| $A$ | flow Jacobian matrix |
| $\mathbf{b}$ | vector of control point coordinates (volume) |
| $\mathbf{B}_{ijk}$ | control point coordinates (local node) |
| $\mathbf{c}$ | vector of constraints |
| $C_D$ | coefficient of drag |
| $C_L$ | coefficient of lift |
| $C_M$ | coefficient of pitching moment |
| $C_p$ | coefficient of pressure |
| $d$ | distance to closest surface boundary |
| $E$ | Young's modulus |
| $\hat{\mathbf{E}}, \hat{\mathbf{F}}, \hat{\mathbf{G}}$ | inviscid flux vectors |
| $\hat{\mathbf{E}}_\mathbf{v}, \hat{\mathbf{F}}_\mathbf{v}, \hat{\mathbf{G}}_\mathbf{v}$ | viscous flux vectors |
| $\mathbf{f}$ | force vector |
| $\mathbf{g}$ | vector of computational mesh coordinates |
| $\mathcal{J}$ | objective function |
| $K$ | stiffness matrix |
| $\mathcal{L}$ | Lagrangian function |
| $m$ | number of mesh movement increments |
| $\mathbf{m}$ | vector of metric terms |
| $M$ | Mach number |
| $\boldsymbol{\mathcal{M}}$ | mesh movement residual vector |
| $N_i, N_j, N_k$ | number of B-spline control points in each coordinate direction |
| $\mathcal{N}$ | B-spline basis function |
| $\mathbf{q}$ | vector of conservative flow variables (mesh volume) |
| $\hat{\mathbf{Q}}$ | vector of conservative flow variables (local node) |
| $\boldsymbol{\mathcal{R}}$ | flow residual vector |
| $Re$ | Reynolds number |
| $T$ | knot vector |
| $\mathbf{v}, \mathbf{X}$ | design variable vectors |
| $\boldsymbol{\lambda}^{(i)}$ | vector of mesh adjoint variables at increment $i$ |
| $\boldsymbol{\psi}$ | vector of flow adjoint variables |

| | |
|---|---|
| $\nu$ | Poisson's ratio |
| $\tilde{\nu}$ | turbulence variable |
| $\xi, \eta, \zeta$ | computational coordinate axes |

## I. Introduction

RISING fuel prices, along with stricter environmental regulations, have contributed to a push within the airline industry for more efficient aircraft that will alleviate fuel costs and reduce greenhouse gas emissions. The next generation of more fuel-efficient aircraft may be the result of incremental improvements to the conventional tube-and-wing configuration [1, 2] or a novel design not yet discovered. In either case, numerical analysis and optimization will be a powerful tool in the design of new aircraft with a reduced environmental footprint. Numerical methods are already being used in the design of the unconventional blended wing-body, double-bubble, and joined-wing configurations [3–7].

The earliest examples of numerical aerodynamic shape optimization can be found in the work of Hicks and Henne [8], who employed finite-difference gradient evaluations and inviscid flow analysis. The use of finite-difference approximations to compute the gradient limited their optimizations to a relatively low number of design variables. The size of the design problem was able to be increased substantially with the advent of adjoint-based methods [9, 10], which make the cost of the gradient evaluation virtually independent of the number of design variables. Since this pioneering work, numerical aerodynamic optimization has become a growing area of research, encompassing a wide variety of design problems with varying degrees of geometric variation relative to an initial geometry. For example, in aerodynamic optimization typical of the detailed design phase, incremental improvements are sought by implementing small-scale changes in the initial geometry. In high-fidelity aerostructural and multidisciplinary optimization, for which an effective aerodynamic shape optimization methodology is an essential component, a wing or aircraft will typically encounter large changes in twist and planform. Finally, in exploratory optimization, the designer often has no knowledge of the types of geometries the optimizer may produce; consequently, very large shape changes can be encountered, and the optimization methodology must be capable of handling them.

The discrete-adjoint approach has been successfully used in a wide range of two-dimensional

aerodynamic shape optimization problems based on the Reynolds-averaged Navier-Stokes (RANS) equations. Anderson and Bonhaus [11] applied the discrete-adjoint gradient evaluation approach to airfoil section optimization problems on unstructured grids in fully turbulent flow; the one-equation Spalart-Allmaras turbulence model was coupled with the Navier-Stokes equations and was fully linearized. Nemec and Zingg [12, 13] developed an efficient gradient-based Newton-Krylov scheme which has been applied to a wide range of two-dimensional turbulent aerodynamic shape optimization problems [14]. Laminar-turbulent transition prediction was incorporated into this tool by Driver and Zingg [15] and used to design a series of natural-laminar-flow airfoils.

Gradient-based three-dimensional turbulent aerodynamic shape optimization is also an active and growing area of research. Hicken and Zingg [16] previously demonstrated the performance of a gradient-based optimization tool based on the three-dimensional Euler equations but pointed out the importance of considering viscous and turbulent effects in order to design under more realistic flow conditions. Elliott made similar assertions in his thesis on optimization based on the two- and three-dimensional Euler and laminar Navier-Stokes equations [17, 18]. Jameson *et al.* [19] used the continuous adjoint approach in the development of SYN107 to optimize wings and wing-body configurations based on the compressible Navier-Stokes equations. Nielsen and Anderson [20] presented examples of discrete-adjoint based optimization based on the three-dimensional RANS equations and the Spalart-Allmaras turbulence model and showed the negative impact that certain simplifications of the linearization have on the gradient accuracy, including freezing the turbulence model. Brezillon *et al.* [21] demonstrated improved performance of the DLR-F6 wing-body configuration with an approach based on the unstructured parallel RANS solver, TAU, and discrete-adjoint gradients; this work was extended to show how the optimization algorithm can be used to reduce the area of flow recirculation at a wing-body junction and to optimize the slat and flap positions for a three-dimensional high-lift configuration [22].

A good summary of the state of the art of RANS-based aerodynamic shape optimization is provided by Epstein *et al.* [23], who applied three state-of-the-art optimization methodologies to the same constrained design problem and demonstrated similar improvements in drag at the main design point and good performance at off-design conditions. Note, however, that the shape changes

in the design problem used in their study are quite small, and no indication is given as to how the methodologies would perform in an optimization with larger shape changes. Overall, RANS-based aerodynamic shape optimization usually involves small changes typical of optimization in the detailed design phase; RANS-based optimization involving large shape changes is still quite rare and requires further research.

Aerostructural and multidisciplinary optimization have been in use for many years [24, 25]; however, the computational costs associated with RANS-based optimization make examples of high-fidelity RANS-based aerostructural and multidisciplinary optimization quite rare. Jameson's work was extended to aero-structural wing planform optimizations [26]. Martins *et al.* [27] applied an aerodynamics model based on the Euler equations and a finite-element structures model to the optimization of a natural-laminar-flow supersonic business jet. Kenway and Kennedy [28, 29] demonstrated a parallelized high-fidelity multidisciplinary algorithm based on an Euler-based flow analysis tool and a finite-element structures model to optimize the CRM aircraft configuration for minimum fuel burn and, separately, minimized maximum take-off weight. Multi-point optimizations were also presented. Recently, Barcelos *et al.* demonstrated the performance of an aerostructural optimization methodology based on the RANS equations [30]. Ghazlane *et al.* [31] applied an aerostructural adjoint method to aerodynamic, aeroelastic, and structural optimizations of the Airbus XRF1 wing-body configuration at a single manoeuvre condition. A multidisciplinary methodology capable of small- and large-scale shape changes based on high-fidelity analysis of aerodynamics, aeroelasticity, structures, and acoustics is in development by Brezillon *et al.* [32] and has been demonstrated for a regional jet configuration with rear fuselage-mounted engines.

This paper describes a methodology for performing aerodynamic shape optimization in turbulent flow. By coupling an integrated geometry parameterization and mesh movement technique with an efficient parallel Newton-Krylov-Schur method for solving the three-dimensional RANS equations, this methodology is effective not only in optimizations typical of the detailed design phase in which incremental improvements are sought, but also in cases with large shape changes. The geometric flexibility and robustness that enables the optimizer to accommodate such a wide range of shape changes will make this methodology a powerful tool as part of a future aerostructural

and multidisciplinary framework, as well as in exploratory optimization.

The paper is divided into the following sections. Section II outlines the integrated geometry parameterization and mesh movement scheme, Section III describes the Newton-Krylov-Schur flow solution algorithm, and Section IV provides details of the discrete-adjoint gradient evaluation. Results are presented in Section V for several optimization studies, including an optimization of the Common Research Model wing geometry, an example in which large geometry changes are encountered, a wing-body-tail configuration where a prescribed spanwise loading constraint is imposed, and a blended wing-body configuration. Conclusions are given in Section VI.

## II. Geometry Parameterization and Mesh Movement

Aerodynamic shape optimization begins with a parameterization in which an initial geometry is represented analytically by a finite number of parameters. There are a number of ways to do this, including Class/Shape Function Transformation (CST) [33], surface nodes [19, 34], CAD packages [21, 35], Freeform Deformation (FFD) [20, 21, 36–38], and basis functions [4, 13–16, 39–41]; the last is the approach used in this work. If a B-spline representation is not available, a B-spline surface is fit to a surface mesh representing the initial geometry.

The integrated geometry parameterization and mesh movement scheme developed by Hicken and Zingg [42] makes use of B-spline tensor volumes that form a coarse approximation of a multi-block structured computational mesh. The initial geometry is thus represented by a set of B-spline surface patches. The B-spline control points that define these patches are used as design variables. When the optimizer alters the positions of the surface control points, the B-spline volume control points are updated accordingly based on the equations of linear elasticity. The computational mesh is then updated algebraically based on the B-spline volume mesh. As there are far fewer control points than mesh nodes, the mesh movement process and associated adjoint solution incur a relatively low computational cost.

This section will summarize the B-spline volume fitting process and will also discuss a set of methods that were developed to create finely-spaced meshes based on initial coarse meshes. Finally, the hybrid mesh movement algorithm will be described.

### A. Fitting Geometries and Multi-Block Meshes Using B-Spline Surfaces and Volumes

A B-spline tensor volume is defined by a set of control points, $\mathbf{B}_{ijk}$, and basis functions of order $p = 4$, $\mathcal{N}$, and can be expressed as

$$\mathbf{x}(\boldsymbol{\xi}) = \sum_{i=1}^{N_i} \sum_{j=1}^{N_j} \sum_{k=1}^{N_k} \mathbf{B}_{ijk} \mathcal{N}_i(\xi) \mathcal{N}_j(\eta) \mathcal{N}_k(\zeta), \tag{1}$$

where $\mathbf{x}(\boldsymbol{\xi})$ represents the set of Cartesian coordinates of the nodes of the mesh volume as a function of the set of curvilinear coordinates $\boldsymbol{\xi} = (\xi, \eta, \zeta) \in \mathbb{R}^3 | \xi, \eta, \zeta \in [0, 1]$. The basis functions in the $\xi$-direction, holding the $\eta$ and $\zeta$ parameters constant, are expressed as

$$\begin{aligned} \mathcal{N}_i^{(1)}(\xi; \eta, \zeta) &= \begin{cases} 1 & \text{if } T_i(\eta, \zeta) \leq \xi < T_{i+1}(\eta, \zeta), \\ 0 & \text{otherwise} \end{cases} \\ \mathcal{N}_i^{(p)}(\xi; \eta, \zeta) &= \left( \frac{\xi - T_i(\eta, \zeta)}{T_{i+p-1}(\eta, \zeta) - T_i(\eta, \zeta)} \right) \mathcal{N}_i^{(p-1)}(\xi; \eta, \zeta) \\ &\quad + \left( \frac{T_{i+p}(\eta, \zeta) - \xi}{T_{i+p}(\eta, \zeta) - T_{i+1}(\eta, \zeta)} \right) \mathcal{N}_{i+1}^{(p-1)}(\xi; \eta, \zeta). \end{aligned} \tag{2}$$

Similar expressions exist for the basis functions in the $\eta$- and $\zeta$-directions, $\mathcal{N}_j^{(p)}(\eta; \zeta, \xi)$ and $\mathcal{N}_k^{(p)}(\zeta; \xi, \eta)$, respectively. The parameter values $(\xi, \eta, \zeta)$ are determined using a chord length parameterization.

The spatially-varying knot values, $T_i(\eta, \zeta)$, in the interior of the B-spline volume are obtained from

$$T_i(\eta, \zeta) = [(1 - \eta)(1 - \zeta)] T_{i,(0,0)} + [\eta(1 - \zeta)] T_{i,(1,0)} + [(1 - \eta)\zeta] T_{i,(0,1)} + [\eta\zeta] T_{i,(1,1)}, \tag{3}$$

with similar expressions used for $T_i(\zeta, \xi)$ and $T_i(\xi, \eta)$. The edge knot values, $T_{i,(0,0)}$, $T_{i,(1,0)}$, $T_{i,(0,1)}$, and $T_{i,(1,1)}$ are constants and, since they are calculated based on the chord-length-based parameter values, also possess a chord-length parameterization.

The initial locations of the B-spline control points are determined using a least-squares fitting routine, which sequentially fits block edges, followed by surfaces and, finally, the internal volume control points. The subset of B-spline control points associated with the aerodynamic surface are

typically used as design variables in an optimization.

B-spline curves obey a strong convex hull property which dictates that a point on a curve of order $p$ must be contained within the convex hull formed by $p$ of its neighbouring control points. Additionally, the movement of a particular control point will produce only localized changes in the curve, which provides local shape control [43]. These properties result in a set of B-spline control points that not only define the computational volume mesh, but also form an approximation of it. This is an important principle that forms the basis for the mesh movement algorithm.

### B. Mesh Refinement Techniques for Turbulent Flow Analysis and Optimization

A computational mesh used in a RANS-based analysis requires fine spacings, particularly in the off-wall direction, in order to accurately capture turbulent flow features, such as the boundary layer. In an Euler-based analysis, the computational mesh may have an off-wall spacing of approximately $10^{-3}$ reference units, whereas that of a mesh used in a RANS-based analysis is approximately $10^{-6}$ reference units. Some additional refinement (approximately one order of magnitude compared to a coarser Euler mesh) is required in the tangential directions on the aerodynamic surfaces as well. Problems arise when fitting the finer computational meshes due to the use of the spatially-varying knot vectors based on the chord length-based parameter values, which cause the B-spline control points to bunch together, and even cross over, in areas near the aerodynamic surface, where the spacings are very fine or where there is a high amount of curvature, and produces a mesh of poor quality. A balance must be struck between creating a well-spaced control-volume mesh and a fitted computational mesh with a sufficient degree of refinement for modelling turbulent flow.

To this end, a dual-option refinement process has been developed that enables grid refinement and redistribution by exploiting the parametric space associated with the B-spline volume. For a given geometry, a computational mesh with coarser spacing is generated. At the beginning of an optimization, each block of the computational mesh is fit with B-spline volumes using a least-squares fitting routine, as previously discussed in Section II A. The coarser computational mesh spacing eliminates bunching and cross-over in the resulting B-spline control-volume mesh. After the B-spline control-volume mesh has been generated, the mesh can be refined using a node-insertion

method, which is referred to as grid refinement. The grid refinement option increases the number of nodes in each coordinate direction by user-specified scaling factors. The entire set of parameter values is re-evaluated using the chord-length based parameterization such that the existing nodes are redistributed to account for the additional nodes.

The second option, which is referred to as grid redistribution, involves the targeted modification of the spacing-control function parameters along specific grid edges. Starting with any fitted computational mesh (which may or may not have already made use of the grid refinement option), the edge spacing parameters corresponding to specific blocks can be adjusted by a set of user-defined scaling factors. This effectively creates spacing refinement by altering the distribution of the nodes along an edge, rather than by inserting additional nodes. The parameter values $\boldsymbol{\xi} = (\xi, \eta, \zeta)$ throughout the remainder of the grid volume are re-evaluated based on the updated edge parameters so that only the block edge spacing parameters need to be altered in order to achieve a distributed grid spacing modification.

A third method, referred to as parameter extraction, has also been implemented. It makes use of a finely-spaced turbulent computational mesh that is canonically equivalent to the coarser mesh and already contains the desired mesh spacing. The grid is read in and the parameter values extracted and applied to the coarser initial mesh; this serves as a variation on the grid redistribution scheme. Instead of manually refining the edge parameter spacings, the nodes of the entire mesh are effectively redistributed based on the turbulent mesh. The cases presented in this work make use of both the grid redistribution method and the parameter extraction method; the method used in each case presented in this work will be explicitly stated.

Since the refinement strategies presented here are all performed in parametric space after the B-spline control-volume mesh has been calculated, any refinement that is performed on the coarse mesh in order to obtain the desired grid spacings has no effect on the control mesh.

### C. Hybrid Mesh Movement

A set of design variables will be updated at each iteration of the optimization. The design variables are typically the coordinates of the surface B-spline control points, referred to as section

shape variables, as well as the angle of attack and planform variables, such as sweep. Planform variables are formed by coupling the coordinates of the B-spline control points; for example, the $x$-coordinates of the surface control points can be coupled to form a single sweep planform variable. Any changes in the control-point coordinates due to the modification of planform variables are independent of the section shape variable changes so that, even if the sections are fixed, the planform variables can still change. Modifications to the surface geometry specified by the optimizer must subsequently be propagated through the B-spline volumes. To achieve this, a method based on the principles of linear elasticity was adapted from the work of Truong *et al.* [44] by Hicken and Zingg [42]. This type of method is computationally expensive; however, the size of the control mesh is typically two orders of magnitude smaller than the flow mesh and thus its movement requires minimal computational time compared to the time required to perform a flow analysis.

The control volumes are modelled as homogeneous, isotropic linear elastic solids, The movement of the control points is governed by

$$\frac{\partial \tau_{ij}}{\partial x_j} + f_i = 0, \tag{4}$$

where $f_i$ is a force vector. The stress tensor, $\tau_{ij}$, and the Cauchy strain tensor $e_{ij}$, are related by the linear expression

$$\tau_{ij} = \frac{E}{1+\nu}\left(e_{ij} + \frac{\nu e_{kk}\delta_{ij}}{1-2\nu}\right) \tag{5}$$

$$e_{ij} = \frac{1}{2}\left(\frac{\partial u_i}{\partial x_j} + \frac{\partial u_j}{\partial x_i}\right) \tag{6}$$

where $u$ represents displacement, $E$ is the spatially-varying Young's modulus, and $\nu = -0.2$ is Poisson's ratio. This approach assumes that the displacements are small; however, to accommodate larger shape changes, the mesh movement is performed in increments, improving the robustness of the method. Five mesh movement increments of equal size are used ($m = 5$). The choice of five increments is neither necessary nor sufficient to ensure that high quality meshes are obtained in all cases. However, we have found this value to be a good balance between speed and robustness

for many optimization problems of interest. The spatially-varying Young's modulus for a given mesh element, $\varepsilon$, at mesh movement increment $i$ is expressed as a function of cell volume and cell orthogonality, or skewness:

$$E_{\varepsilon}^{(i)} = \frac{\Phi_{\varepsilon}^{(i-1)}}{\Phi_{\varepsilon}^{(0)} V_{\varepsilon}^{(i-1)}}, \qquad i = 1, 2, \ldots, m, \tag{7}$$

where $V_{\varepsilon}$ is the element volume and $\Phi_{\varepsilon}$ is a cell orthogonality measure. The Young's modulus is based on the cells of the control mesh. In order for this approach to be effective, these must reflect those of the flow mesh.

Equation (4) is discretized on the control mesh using a finite-element method with trilinear elements. Incorporating the incremental mesh movement results in the linear system

$$\mathcal{M}^{(i)}(\mathbf{b}^{(i-1)}, \mathbf{b}^{(i)}) = K^{(i)}(\mathbf{b}^{(i-1)})[\mathbf{b}^{(i)} - \mathbf{b}^{(i-1)}] - \mathbf{f}^{(i)} = 0, \qquad i = 1, \ldots, m, \tag{8}$$

where $\mathcal{M}^{(i)}$ is the mesh movement residual at increment $i$, $K^{(i)}$ is the sparse, symmetric, positive-definite stiffness matrix, $\mathbf{b}^{(i)}$ is a block-column vector containing the control-point coordinates at increment $i$, and $\mathbf{f}^{(i)}$ is a force vector that is defined implicitly based on the movement of the control points on the aerodynamic surfaces. A node associated with a deformed boundary has a force contribution equal to the product of its element stiffness and its displacement. The remaining entries in the force vector are zero. Note that the term $\mathbf{B}_{\mathrm{ijk}}$ in (1) represents a set of coordinates for a single control point, a lower-case $\mathbf{b}$ term in (8) represents a block-column vector of the coordinates for all control points within a B-spline volume, and $\mathbf{b}_{\mathrm{s}}$ represents a subset of $\mathbf{b}$, containing the surface control-point coordinates.

The linear system (8) is solved using the conjugate gradient method preconditioned with ILU(1) [45]. The convergence criterion is a reduction in the $L_2$ norm of the residual to a relative tolerance of $10^{-12}$. The fine mesh is updated using an algebraic approach based on the B-spline volume basis functions in (1). This integrated approach remains efficient even for large multi-block meshes, requiring minimal CPU time for the mesh movement and mesh adjoint systems relative to the time required to solve the flow and compute the gradient, while maintaining good mesh quality. The

mesh adjoint system will be discussed in more detail in Section IV.

## III. Newton-Krylov-Schur Flow Solver

At its core, an optimization algorithm must have an efficient, accurate method of analyzing the flow around an aerodynamic body. Given inaccurate data from the flow solver, the optimizer can not produce a valid optimum for the specified flow conditions. Efficiency and robustness are key attributes of the flow solver, since the flow analysis is carried out many times over the course of an optimization, and the geometry can be expected to undergo large changes in many cases. The Newton-Krylov-Schur method used to obtain the flow solutions for the high-fidelity aerodynamic shape optimization algorithm will be summarized briefly in this section. The parallel implicit flow solution algorithm was developed by Hicken and Zingg [46] for the solution of the three-dimensional Euler equations and adapted by Osusky and Zingg [47] to solve the three-dimensional Reynolds-Averaged Navier-Stokes equations.

The algorithm solves the three-dimensional Reynolds-averaged Navier-Stokes (RANS) equations, given in curvilinear coordinates by [48]

$$\partial_t \hat{\mathbf{Q}} + \partial_\xi \hat{\mathbf{E}} + \partial_\eta \hat{\mathbf{F}} + \partial_\zeta \hat{\mathbf{G}} = \frac{1}{Re}\left(\partial_\xi \hat{\mathbf{E}}_\mathbf{v} + \partial_\eta \hat{\mathbf{F}}_\mathbf{v} + \partial_\zeta \hat{\mathbf{G}}_\mathbf{v}\right), \tag{9}$$

where the inviscid fluxes are represented by $\hat{\mathbf{E}}$, $\hat{\mathbf{F}}$, and $\hat{\mathbf{G}}$, and the viscous fluxes by $\hat{\mathbf{E}}_\mathbf{v}$, $\hat{\mathbf{F}}_\mathbf{v}$, and $\hat{\mathbf{G}}_\mathbf{v}$. The vector $\hat{\mathbf{Q}}$ represents the set of conservative flow variables. The Spalart-Allmaras turbulence model adds an additional variable and partial differential equation; it is treated in a fully-coupled manner.

The governing equations are discretized on multi-block structured grids using second-order-accurate summation-by-parts (SBP) operators. Boundary conditions and inter-block coupling are enforced weakly using simultaneous approximation terms (SATs) [49–52]; this approach requires only boundary information from neighbouring blocks, minimizing computational overhead. Further details of the SBP-SAT implementation can be found in references [46, 47, 53–58].

Applying an implicit-Euler time-marching scheme with local time linearization to the system of ordinary differential equations resulting from the spatial discretization produces a large, sparse

system of linear equations, which is solved using flexible GMRES (FGMRES). Preconditioning is performed using an approximate-Schur preconditioner [59]. The time step is increased as the residual is reduced such that an inexact-Newton method is obtained. An approximate-Newton start-up phase is used to determine a suitable initial iterate for the inexact-Newton phase, which then reduces the residual to a prescribed relative tolerance of $10^{-10}$. A complete description of the flow solver can be found in [47].

## IV. Gradient Evaluation

The optimization problem can be expressed in the general form

$$\begin{aligned} &\min \quad \mathcal{J}(\mathbf{v}, \mathbf{b}^{(m)}, \mathbf{q}) \\ &\text{w.r.t } \mathbf{v} \\ &\text{s.t.} \quad \mathbf{c_i}(\mathbf{v}, \mathbf{b}^{(m)}, \mathbf{q}) \leq \mathbf{0},\, \mathbf{c_e}(\mathbf{v}, \mathbf{b}^{(m)}, \mathbf{q}) = \mathbf{0}, \end{aligned}$$

where $\mathcal{J}$ represents the objective function to be minimized (typically drag), $\mathbf{v}$ represents a set of design variables, $\mathbf{q}$ is a vector of flow variables, and $\mathbf{c_i}$ and $\mathbf{c_e}$ represent sets of inequality and equality constraints, respectively. Included in the constraints are the discrete flow equations and mesh movement equations, as well as other nonlinear aerodynamic and geometric constraints, such as lift and volume. When $\mathbf{v}$ contains section variables, it represents a subset of $\mathbf{b}^{(m)}$, the volume control points. The angle of attack, as well as planform design variables like sweep, may also be included in the vector of design variables.

The optimizer requires the gradient of the objective function and constraints. Gradients are obtained in a sequential manner. The equations governing the flow are first solved as described in Section III. The next step is the solution of the flow and mesh adjoint systems.

### A. Flow Adjoint System

The flow adjoint variables, $\boldsymbol{\psi}$, are obtained from the system

$$A^T \boldsymbol{\psi} = -\left(\frac{\partial \mathcal{J}}{\partial \boldsymbol{q}}\right)^T, \tag{10}$$

where the flow Jacobian matrix $A = \frac{\partial \boldsymbol{\mathcal{R}}}{\partial \boldsymbol{q}}$ is obtained analytically, as is the $\frac{\partial \mathcal{J}}{\partial \boldsymbol{q}}$ term on the right-hand side. The global flow residual vector is represented by $\boldsymbol{\mathcal{R}}$.

In order to capture shocks in transonic flow conditions, a shock sensor is included within the artificial dissipation model. The shock sensor is active in regions where the flow experiences large pressure changes. Due to the complexity of the shock sensor formulation and the increase in storage requirements that a full linearization produces, the shock sensor is often treated as a constant in the evaluation of the flow Jacobian. It was found that, while omitting the shock sensor linearization introduces small errors in inviscid cases [60] and two-dimensional viscous cases [13], the amount of error was determined to be acceptable when the final solutions were shock-free. Such errors in the total gradient are much more problematic for cases in which the final solution is not shock-free. Consequently, a full linearization of the shock sensor was implemented as part of this work [61].

The flow adjoint system is preconditioned with ILU(2) and solved to a relative tolerance of $10^{-10}$ using a simplified and flexible variant of GCROT (Generalized Conjugate Residual with Orthogonalization and Truncation), a nested GMRES-type solver that recycles Krylov subspaces in order to reduce memory requirements [62–64]. This method is preferred over restarted GMRES when deep convergence is required.

### B. Mesh Adjoint System

The mesh adjoint equation corresponding to the final increment of mesh movement, given by

$$\left(\frac{\partial \boldsymbol{\mathcal{M}}^{(m)}}{\partial \boldsymbol{b}^{(m)}}\right)^T \boldsymbol{\lambda}^{(m)} = -\left(\frac{\partial \mathcal{J}}{\partial \boldsymbol{b}^{(m)}}\right)^T - \left(\frac{\partial \boldsymbol{\mathcal{R}}}{\partial \boldsymbol{b}^{(m)}}\right)^T \boldsymbol{\psi}, \tag{11}$$

is solved for the mesh adjoint variables $\boldsymbol{\lambda}^{(m)}$. In order to make (11) easier to solve, the right-hand side is expanded using the chain rule, resulting in the modified equation

$$-\left(\frac{\partial \mathcal{J}}{\partial \boldsymbol{b}^{(m)}}\right)^T - \left(\frac{\partial \boldsymbol{\mathcal{R}}}{\partial \boldsymbol{b}^{(m)}}\right)^T \boldsymbol{\psi} = -\left(\frac{\partial \boldsymbol{g}}{\partial \boldsymbol{b}^{(m)}}\right)^T \left[\left.\frac{\partial \mathcal{J}}{\partial \boldsymbol{g}}\right|_{\boldsymbol{m}} + \left(\left.\frac{\partial \mathcal{J}}{\partial \boldsymbol{m}}\right|_{\boldsymbol{g}} + \boldsymbol{\psi}^T \frac{\partial \boldsymbol{\mathcal{R}}}{\partial \boldsymbol{m}}\right) \frac{\partial \boldsymbol{m}}{\partial \boldsymbol{g}} + \boldsymbol{\psi}^T \left.\frac{\partial \boldsymbol{\mathcal{R}}}{\partial \mathbf{g}}\right|_m\right]^T. \tag{12}$$

This reformulation results in a system that requires the storage of only vector-matrix and matrix-vector products. Neither the $\frac{\partial \mathcal{J}}{\partial \boldsymbol{b}^{(m)}}$ term nor the $\frac{\partial \boldsymbol{\mathcal{R}}}{\partial \boldsymbol{b}^{(m)}}$ term is formed explicitly. The vectors

$\boldsymbol{g}$ and $\boldsymbol{b}$ represent the Cartesian grid coordinates and B-spline volume control-point coordinates, respectively. The metric terms arising from the coordinate transformation are represented by $\boldsymbol{m}$. The linearizations that constitute the right-hand side of (12) are obtained analytically, and the left-hand side of (11) can be expressed as the symmetric stiffness matrix at increment $m$, $\boldsymbol{K}^{(m)}$, which is also derived analytically.

The system (12) is solved to a relative tolerance of $10^{-12}$ using the conjugate gradient method preconditioned with ILU(1). Once the vector of mesh adjoint variables at the last mesh movement increment has been computed, the mesh adjoint variables corresponding to the remaining increments, $\boldsymbol{\lambda}^{(i)}|_{i=1}^{m-1}$, can be obtained sequentially from

$$\left(\frac{\partial \boldsymbol{\mathcal{M}}^{(i)}}{\partial \boldsymbol{b}^{(i)}}\right)^T \boldsymbol{\lambda}^{(i)} = -\left(\frac{\partial \boldsymbol{\mathcal{M}}^{(i+1)}}{\partial \boldsymbol{b}^{(i)}}\right)^T \boldsymbol{\lambda}^{(i+1)}, i \in \{m-1, m-2, \ldots, 1\}. \tag{13}$$

The left-hand side of (13) is the symmetric stiffness matrix at increment $i$, $\boldsymbol{K}^{(i)}$. The right-hand side matrix is obtained using the complex-step method due to the dependence of $\boldsymbol{\mathcal{M}}^{(i+1)}$ on $\mathbf{b}^{(i)}$, the vector of control point coordinates at increment $i$ of the mesh movement. The complex-step evaluation requires minimal computational time, as it is only applied to the coarse control mesh. The system (13) is also solved to a tolerance of $10^{-12}$ using the preconditioned conjugate gradient method preconditioned with ILU(1).

### C. Lagrangian Merit Function

The flow and mesh adjoint equations are incorporated into a Lagrangian function of the form

$$\mathcal{L}(\mathbf{v}, \mathbf{b}^{(m)}, \mathbf{q}, \boldsymbol{\lambda}^{(i)}|_{i=1}^{m}, \boldsymbol{\psi}) = \mathcal{J}(\mathbf{v}, \mathbf{b}^{(m)}, \mathbf{q}) + \sum_{i=1}^{m} \boldsymbol{\lambda}^{(i)T} \boldsymbol{\mathcal{M}}^{(i)}(\mathbf{v}, \mathbf{b}^{(i-1)}, \mathbf{b}^{(i)}) + \boldsymbol{\psi}^T \boldsymbol{\mathcal{R}}(\mathbf{v}, \mathbf{b}^{(m)}, \mathbf{q}). \tag{14}$$

The gradient of the Lagrangian function, $\mathcal{L}$, with respect to the design variables, $\mathbf{v}$, is of the form

$$\mathcal{G} = \frac{\partial \mathcal{L}}{\partial \mathbf{v}} = \frac{\partial \mathcal{J}}{\partial \mathbf{v}} + \sum_{i=1}^{m} \left(\boldsymbol{\lambda}^{(i)T} \frac{\partial \boldsymbol{\mathcal{M}}^{(i)}}{\partial \mathbf{v}}\right) + \boldsymbol{\psi}^T \frac{\partial \boldsymbol{\mathcal{R}}}{\partial \mathbf{v}}. \tag{15}$$

### D. Gradient-Based Constrained Optimization

Optimizations are carried out using the sparse sequential quadratic programming (SQP) algorithm SNOPT [65], which is capable of handling linear and nonlinear constraints. Linear constraints can be used to couple B-spline control points to a smaller subset of control points, effectively reducing the number of geometric degrees of freedom. For example, the $x$-coordinates of the control points can be coupled to the movement of a single leading-edge coordinate at the wing tip. SNOPT is able to satisfy linear constraints exactly.

Nonlinear constraints, such as lift, volume, or area, are solved to a user-specified tolerance, typically $1 \times 10^{-6}$. In the case of nonlinear aerodynamic constraints, the gradient evaluation, including the solution of the flow and mesh adjoint equations, must be repeated for each constraint. The nonlinear constraints are included in SNOPT's Lagrangian merit function, which is not to be confused with (14); if the constraints are satisfied, then the merit function is equal to the objective function, $\mathcal{J}$.

The use of a gradient-based optimization method means that the results presented in this paper are local optima and are not guaranteed to be the global optimum. A gradient-based approach does, however, have the benefit of lower computational cost and convergence times compared to many gradient-free methods [66]. Hybrid methods have the potential to combine the desirable characteristics of both gradient-based and gradient-free methods and enable the designer to obtain a global optimum at a lower computational cost relative to a purely gradient-free approach. Chernukhin and Zingg [67] developed two novel gradient-based global optimization strategies and applied them to multi-modal three-dimensional aerodynamic design problems based on the Euler equations. The first approach makes use of Sobol sequencing to explore the design space and obtain a set of initial geometries which are then optimized with a gradient-based algorithm. The second is a hybrid approach combining features of both genetic and gradient-based optimization algorithms; offspring resulting from the genetic algorithm are further improved with a gradient-based optimization before the next generation of offspring are determined. The present methodology can be used with either of these two approaches.

Following the gradient evaluation, SNOPT updates the design variables. The B-spline control

volume mesh and computational mesh are updated accordingly, as described in Section II C. The sequence of steps described in this section constitute one design iteration. The methodology then returns to the solution of the flow equations to begin another design iteration.

### E. Planform Variables

Another method of coupling the B-spline control points to reduce the number of geometric degrees of freedom is the use of planform design variables. These variables are defined in a similar manner to the linear constraints in that the equations coupling the control points are the same. Planform variables, however, not only reduce the number of degrees of freedom, but also reduce the total number of design variables seen by SNOPT, which can help improve the speed and final level of convergence.

Consider the leading-edge sweep design variable, $\Delta\Gamma_{\mathrm{LE}}$, which is given by

$$\Delta\Gamma_{\mathrm{LE}} = \tan^{-1}\frac{\Delta x_{\mathrm{LE}}}{\Delta y_{\mathrm{LE}}}, \tag{16}$$

where the LE subscript refers to the leading-edge, $\Delta y_{\mathrm{LE}} = (y_{\mathrm{tip}} - y_{\mathrm{root}})\big|_{\mathrm{LE}}$ is the semi-span of the wing, and $\Delta x_{\mathrm{LE}}$ is a translation of the control point at the leading-edge wing tip in the $x$-direction. Note that the changes in the planform variables are applied to the B-spline control mesh; thus, the $x$ and $y$ coordinates in this example refer to the coordinates of the B-spline control points. The $x$-direction translation can be expressed as

$$\Delta x_{\mathrm{LE}} = \Delta y_{\mathrm{LE}} \tan\Delta\Gamma_{\mathrm{LE}}. \tag{17}$$

If the trailing-edge sweep angle is also a design variable, a similar expression exists for $\Delta\Gamma_{\mathrm{TE}}$. The locations of the interior surface control points are determined using a linear interpolation based on the leading-edge and trailing-edge control points. The translation in the $x$-direction of a control point, represented by $x_p$, can be expressed as

$$\Delta x = \Delta x_{\mathrm{LE}}\frac{x_{\mathrm{TE}} - x_p}{x_{\mathrm{TE}} - x_{\mathrm{LE}}} + \Delta x_{\mathrm{TE}}\frac{x_p - x_{\mathrm{LE}}}{x_{\mathrm{TE}} - x_{\mathrm{LE}}}. \tag{18}$$

The use of planform design variables necessitates the use of an extra term in (15) that communicates the relationship between the planform variables and the control points that form them within the context of the objective gradient. This term is of the form

$$\frac{\partial \mathcal{J}}{\partial \mathbf{X}_{\text{pdv}}} = \frac{\partial \mathcal{J}}{\partial \mathbf{b}^{(m)}} \frac{\partial \mathbf{b}^{(m)}}{\partial \mathbf{X}_{\text{pdv}}}, \tag{19}$$

where $\frac{\partial \mathbf{b}^{(m)}}{\partial \mathbf{X}_{\text{pdv}}}$ is a sparse matrix containing the derivatives of the offsets with respect to the planform variables.

Similar expressions can be derived for the leading-edge and trailing-edge dihedral angles, linear twist angle, and semi-span. Sweep, dihedral, twist, and angle of attack design variables are defined in terms of radians during the optimization.

### F. Region Design Variables

In addition to the design variables previously described in Section IV E, an alternative design variable definition is implemented, termed 'region design variables' (RDVs). This formulation is used for the cases presented in Sections V D and V E. This definition aims to provide variables which can be easily and intuitively defined and whose definition for a wide range of surface patch geometries and topologies is transparent to the user.

The surface patches are grouped into 'regions', with regions being grouped to form 'components'. This subdivision is shown in Fig. 1a) for a sample transport aircraft. The design variables of each region are defined in a coordinate system local to that region. This allows for better control of local parameters, such as airfoil sections, while global geometric changes occur, such as dihedral. Figure 1b) shows a sample region and some of the variables which control the shape within the local coordinate system. These variables allow for the definition and control of planform and section parameters. The variables shown in Fig. 1b) are non-intuitive to the user, who is primarily concerned with parameters such as taper, sweep, twist, etc. Instead of using these intuitive parameters as design variables directly, the non-intuitive set of Fig. 1b) is used, as this allows for as many constraints as possible to be expressed as linear constraints, which SNOPT can satisfy exactly at the start of the optimization. These non-intuitive RDVs are coupled through a series of relations to provide

intuitive parameters, such that the designer can specify intuitive parameters and their bounds, and the expression of these in terms of regions variables is transparent to the user.

The RDVs in each region, $R$, define the control point coordinates of that region in the local space ($\bar{\mathbf{X}}_R$), and these are transformed to the corresponding control point locations in global space ($\mathbf{X}$) via the transform

$$\mathbf{X} = \sum_{r=1}^{R-1} \begin{bmatrix} \bar{x}_{\mathrm{LE}}^{\mathrm{tip}} \\ \bar{b}\cos\Gamma \\ \bar{b}\sin\Gamma \end{bmatrix}_r + \phi_x(\Gamma_R)\ \bar{\mathbf{X}}_R$$

where $\Gamma$ is the dihedral angle of each region, and $\phi_x$ is the rotation matrix about the global streamwise axis.

For full aircraft configurations, two additional geometric control features are required. The first is the definition and control of distinct features which are to be designed, such as the wing and tail of the transport aircraft in Fig. 1a). This introduces the concept of 'components', which are simply groupings of regions which form topologically distinct geometric entities. Global translation and rotation variables are associated with each component, such that changes in location and pitch of the wing and tail are handled. The second geometric control feature is a method for handling the interaction of free and fixed surfaces, such as a wing and fuselage, during the optimization. Currently, no design variables are associated with the fuselage surface, and the fuselage surface is driven by geometric changes made to the wing surface. Changes at the wing root are propagated along the fuselage surface via the relation

$$\mathbf{x}_k = \mathbf{x}_k^0 + (\mathbf{x}_1 - \mathbf{x}_1^0)\left[\frac{1+\cos(\pi S_k)}{2}\right]^{\beta} \qquad \text{for} \quad k = 2 \ldots k_{\max}$$

where $\mathbf{x}$ is the 3-vector of control point coordinates, and $k$ is the control point index along control mesh grid lines emanating from the component root as shown in Fig. 1c). The case of $k = 1$ corresponds to the control points at the fuselage-wing junction that are controlled by design variables on the wing region. The '0' superscript corresponds to the geometry at the start of the optimization.

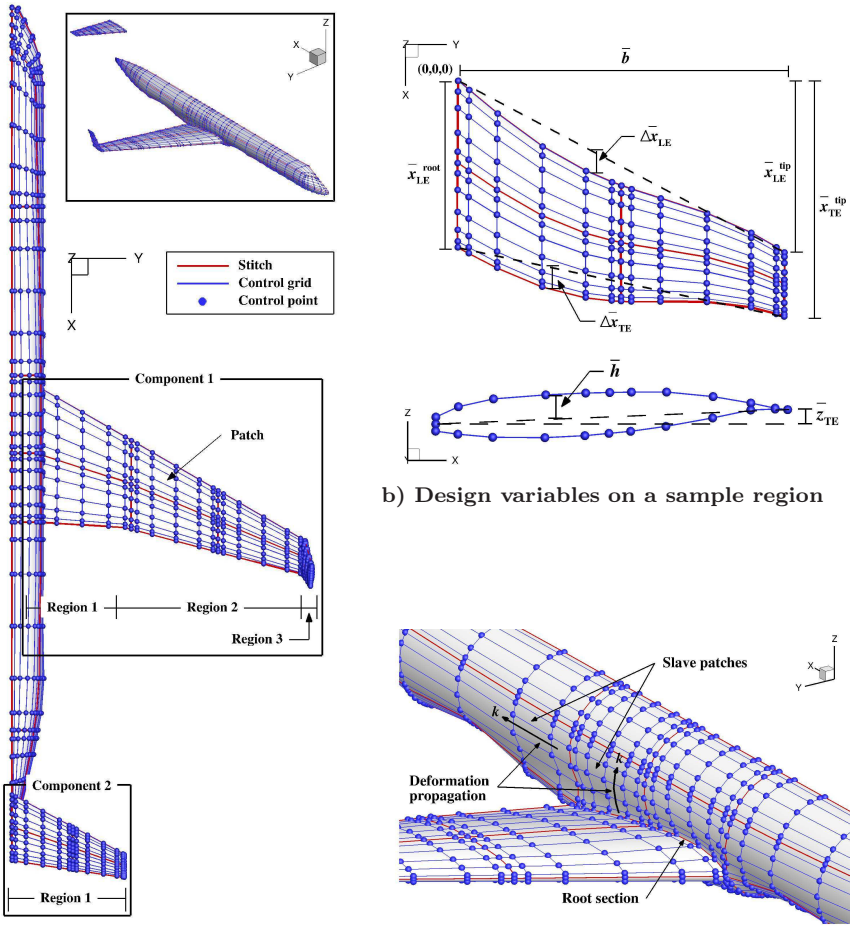


a) Breakdown of surface patches into components and region

b) Design variables on a sample region

c) Design variables on a sample region

**Fig. 1 Sample region design variable definition on a transport aircraft**

The variable $S_k$ is the normalized arc-length along a given control mesh line emanating from the wing root, and $k_{\max}$ is the number of control points along the surface over which the propagation is to occur. The parameter $\beta$ is used to control the degree to which geometric changes at the fuselage-wing junction propagate along the fuselage surface. Large values are desirable as they localize shape changes to near the fuselage-wing junction, yet they can lead to self-intersection of the fuselage surface for large wing root geometry changes. A value of $\beta = 4$ serves as a good compromise for the typical level of geometric deformations.

### G. Design Variable Scaling

The order of magnitude of the objective gradient components corresponding to each individual design variable typically varies by up to four orders of magnitude; typical values can be as low as

$10^{-5}$ and can be as high as $10^{0}$. It has been found that using design variable scaling can improve convergence [68], particularly in cases with large numbers of geometric design variables, such as a case that allows the $z$-coordinates of the B-spline control points to vary. If a gradient component is very small and close to the convergence tolerance, the optimizer will focus on varying the control points with higher gradient components in order to reduce the total gradient.

There are three groups of design variables, each of which can be scaled by a different factor. The subset of B-spline control point coordinates which are free to move, referred to as geometric design variables, are typically scaled by a factor of 100.0. Planform design variables are scaled by a factor of 5.0. The angle of attack design variable is not typically scaled. The choice of design variable scaling can have a significant effect on optimization convergence [68] and is difficult to analyze. Hence it is suggested that more work be done in this area. The present choices are based on a limited amount of experimentation, and it is not to be inferred that they are in any sense optimal.

### H. Spanwise Lift Distribution Constraint

The substantial computational expense associated with high-fidelity aerostructural optimization and the current-era scarcity of algorithms with this capability motivates an alternative approach to wing design that addresses both aerodynamic and structural requirements and can be implemented in an algorithm with only aerodynamic shape optimization capability. In the optimization case presented in Section V D a prescribed spanwise lift distribution on the wing of an aircraft is enforced to ensure that the optimal wing design is feasible with respect to structural considerations. The prescribed lift distribution may be obtained from a less expensive design tool such as a medium-fidelity aerostructural optimization algorithm. In the absence of a lift-distribution constraint an aerodynamic shape optimization can be expected to produce an elliptical lift-distribution that is not optimal once wing weight is taken into consideration.

A prescribed lift distribution can be enforced by subjecting an aerodynamic shape optimization to a constraint function given by

$$C(\mathbf{X}) \quad = \quad \sum_{i=1}^{n} \left[ L^{*}(y_i) - L(\mathbf{X}, y_i) \right]^2 \quad = \quad 0 \tag{20}$$

where the prescribed lift distribution is represented by a discrete set of target sectional lift values $L^*(y_i)$ defined over a range of spanwise locations given by $y_i$. Sectional lift values at the current design iteration are given by $L(\mathbf{X}, y_i)$, where $\mathbf{X}$ represents a set of geometric and local angle-of-attack design variables. In practice the spanwise locations $y_i$ used in the constraint function are coincident with the spanwise locations of geometric design variables that control section shapes.

### I. Optimization Convergence Criteria

A successful optimization using SNOPT will satisfy the KKT conditions to within a certain tolerance. The nonlinear constraints must be satisfied to a user-specifed tolerance such that

$$\frac{\|\boldsymbol{c}\|_\infty}{\|\boldsymbol{v}\|_2} \leq \varepsilon, \tag{21}$$

where $\boldsymbol{c}$ represents the constraint equations, and $\boldsymbol{v}$ are the scaled design variables. The tolerance parameter $\varepsilon$ is typically set to $1 \times 10^{-6}$ for the cases presented in this work.

The gradient of the Lagrangian function must also be sufficiently small, satisfying

$$\frac{\|\boldsymbol{g}\|_\infty}{\|\boldsymbol{\varphi}\|_2} \leq \varepsilon, \tag{22}$$

where $\boldsymbol{g}$ represents the gradient, and $\boldsymbol{\varphi}$ are the adjoint variables within SNOPT's internal Lagrangian merit function. The tolerance $\varepsilon$ for the gradient is typically $1 \times 10^{-5}$; however, this level of convergence is often not achieved.

## V. Results

Results are presented in this section which demonstrate the performance of the optimization methodology in a variety of conditions. A study of the Common Research Model (CRM) wing geometry in turbulent transonic flow conditions presents optimizations typical of the detailed design phase and seeks incremental improvements to a given initial geometry such that drag is minimized at a target lift coefficient. A single-point drag minimization is presented for a blended wing-body configuration at cruise conditions in order to demonstrate the performance of the methodology when

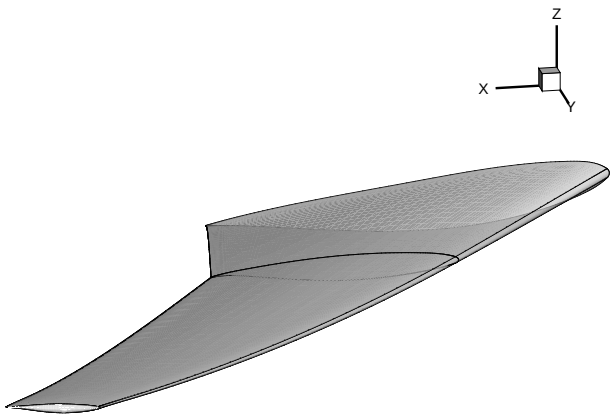


**Fig. 2 Blunt trailing-edge CRM wing geometry**

considering unconventional geometries.

### A. Common Research Model Wing Geometry

A lift-constrained drag minimization is undertaken for the Common Research Model (CRM) wing-only geometry, shown in Fig. 2, which was obtained from the full wing-body configuration studied at the Fourth and Fifth Drag Prediction Workshops [69, 70]. This wing features a blunt trailing edge. The wing-only geometry was obtained by starting with the full wing-body configuration and deleting the fuselage. This leaves the wing root a distance of 120.52 inches from the original symmetry plane. The leading edge of the wing root is then translated to the origin and all grid coordinates are scaled by the mean aerodynamic chord (MAC), which has a value of 275.8 inches. At this stage, the entire root chord does not lie exactly on the symmetry plane; additionally, grid generation can also introduce non-zero symmetry plane coordinates. Consequently, after the computational mesh is generated using ICEM [71], a post-processing script is applied to all nodes on the symmetry plane to ensure that they are at $y = 0$.

The O-O topology computational mesh used for parameterization and mesh movement is made up of 18 blocks and 3.38 million nodes. Flow analysis is performed on a mesh that is created by splitting each block of the parameterization mesh into 8 sub-blocks, resulting in a 144-block, 3.57

million-node mesh. The MAC is used as the reference length. Applying the grid redistribution technique produces an off-wall spacing of $2.56 \times 10^{-6}$ reference units, resulting in an average $y^+$ value of 1.0 at the first node off of the surface.

The wing geometry has 9 surface patches: 2 each on the upper and lower surfaces, 2 each along the leading edge and blunt trailing edge, and one cap patch at the wing tip. The leading-edge patches (one for the inboard section and one for the outboard) are required in order to match with the blunt trailing-edge patches, and also serve as a method of better capturing the curvature of the leading edge. Each surface patch is parameterized with 7 control points in the chordwise direction and 5 in the spanwise direction, with the exception of the patches along the leading and trailing edges, which have 5 control points in the chordwise direction. The control points at the trailing edge are fixed, as is the control point at the leading-edge root, while the remaining control points are allowed to move vertically. Along with the angle of attack, this results in 150 design variables.

For comparison, two additional wings are included in this study. The first is the CRM wing geometry with a sharp trailing edge, as opposed to a blunt trailing edge, which allows for a comparison between an Euler-based optimization and a RANS-based optimization (the flow near a blunt trailing edge is unsuited to the inviscid approximation). The second wing has the same planform as the CRM wing, but is given NACA0012 sections (with a sharp trailing edge) rather than the section shapes of the original CRM geometry. In order to obtain the sharp trailing edge, a B-spline representation of the original CRM wing geometry is obtained from the IGES file and modified using an external script. The B-spline control points are linearly tapered at each spanwise station over the last 10% of the chord to create a sharp trailing edge located at the average $z$-coordinate between the upper and lower edges of the original blunt trailing edge. This alteration to the geometry requires a different blocking structure in the computational mesh compared to that of the blunt trailing-edge geometry, as an O-O topology is not feasible with the introduction of the sharp trailing edge. The two additional geometries consequently use a C-H topology mesh which is made up of 10 surface patches; the upper surface, lower surface, and cap each have two patches. The inboard and outboard sections of the leading edge now also have two patches each. The leading-edge and cap patches are parameterized with 5 control points in the chordwise direction and 5 in the spanwise direction, while

**Table 1 Mesh data for CRM analysis**

| | Parameterization Blocking | | | | | Flow Analysis Blocking | |
|---|---|---|---|---|---|---|---|
| | **Blocks** | **Nodes** | **Patches** | **Off-wall d** (ref. units) | $y^+_{avg}$ | **Blocks** | **Nodes** |
| **blunt TE** | 18 | $3.38 \times 10^6$ | 9 | $5.15 \times 10^{-6}$ | 1.0 | 144 | $3.57 \times 10^6$ |
| **sharp TE** | 24 | $11.05 \times 10^6$ | 10 | $2.58 \times 10^{-6}$ | 0.54 | 192 | $11.50 \times 10^6$ |
| **NACA0012** | 24 | $11.05 \times 10^6$ | 10 | $2.62 \times 10^{-6}$ | 0.50 | 192 | $11.50 \times 10^6$ |

**Table 2 Geometric data for CRM analysis**

| **Wing Geometry** | | | | | |
|---|---|---|---|---|---|
| | | *blunt TE* | *sharp TE* | *NACA0012* | |
| **Volume** | $V$ | 0.262 | 0.263 | 0.287 | cubed ref. units |
| **Surface Area** | $S_{\text{srf}}$ | 3.50 | 3.50 | 3.52 | squared ref. units |
| **Projected Area** | $S_{\text{prj}}$ | 3.41 | 3.41 | 3.41 | squared ref. units |
| **Root Chord** | $c_{\text{root}}$ | 1.69 | 1.69 | 1.69 | ref. units |
| **MAC** | $c_{\text{MAC}}$ | 1.00 | 1.00 | 1.00 | ref. units |
| **Span** | b | 3.76 | 3.76 | 3.76 | ref. units |

the remaining patches on the upper and lower surfaces have 7 and 5 control points in the chordwise and spanwise directions, respectively. This parameterization yields 206 design variables, including the angle of attack.

Data pertaining to the computational meshes used for the three initial wing geometries are summarized in Table 1. Geometrical data for the three initial geometries are presented in Table 2. Note that the volume of the sharp trailing-edge geometry is slightly higher than that of the blunt trailing edge, despite the fact that the opposite is expected. This is the result of the requirement of a different mesh topology for the sharp trailing edge; after the B-spline fit is performed, this small numerical inconsistency is produced.

Two cases are undertaken for each of the three initial wing geometries considered in this study. In the first case, drag is minimized subject to a nonlinear equality lift constraint given by $C_L = 0.5$ and a nonlinear inequality pitching moment constraint given by $C_M \geq -0.17$. The second case considers only the drag objective and lift constraint, with no consideration of the pitching moment. In both cases, a nonlinear inequality constraint is used to maintain the volume of the wing at a value that is greater than or equal to its initial value. In the case of the wing with NACA0012 sections, the target volume is specified as that of the sharp trailing-edge CRM configuration. A linear inequality thickness constraint prevents the vertical separation distance between any two control points in the

**Table 3 Initial lift, drag, and moment data for CRM analysis**

| | Wing Geometry | | |
|---|---|---|---|
| | *Blunt TE* | *Sharp TE* | *NACA0012* |
| $C_L$ | 0.500 | 0.500 | 0.500 |
| $C_D$ | 0.0212 | 0.0205 | 0.0681 |
| $C_M$ | -0.1740 | -0.1628 | -0.0114 |
| $\alpha$ (°) | 2.32 | 2.41 | 5.40 |

same vertical plane from going below 25% of its initial value.

Case 1 refers to the lift-constrained drag minimization with the nonlinear inequality pitching moment constraint. Case 2 refers to the optimization run as a lift-constrained drag minimization problem with no consideration of the pitching moment. Apart from the use of the pitching moment constraint, the two cases are identical.

Flow analyses are performed at a Mach number of 0.85, a Reynolds number of 5 million (based on the reference length), and an initial angle of attack of 2.2°. Pitching moments are taken about the point (1.2077, 0.0, 0.007669) MAC units relative to an origin located at the leading-edge root. These conditions and conventions are consistent with those used in the Drag Prediction Workshop analysis. The lift, drag, and pitching moment coefficients corresponding to the three initial geometries at the specified Mach and Reynolds numbers are presented in Table 3. The angles of attack have been adjusted so that each geometry can be compared at the target lift coefficient of $C_L = 0.5$. All coefficients are calculated using the projected area as the reference area, $S_{\text{ref}} = S_{\text{prj}} = 3.407$ squared reference units.

The coefficients of lift, drag, and pitching moment are displayed in Table 4 for the three initial geometries and the corresponding optimization results from Cases 1 and 2. The lift-to-drag ratio improves by 7-10% in the blunt trailing-edge and sharp trailing-edge cases, while the ratio improved by over 200% over the initial geometry with NACA0012 sections. In each case, the constraints on lift and volume are satisfied, as is the pitching moment constraint for the Case 1 results. The geometries produced in the Case 2 optimizations produce slightly lower drag coefficients compared to the Case 1 geometries and produce larger nose-down positive pitching moment coefficients. Convergence histories for the three initial geometries are presented in Figs. 3, 4, and 5. In these plots, feasibility

**Table 4 Lift, drag, and moment data for CRM wing optimizations**

| | Blunt TE | | | Sharp TE | | | NACA0012 | | |
|---|---|---|---|---|---|---|---|---|---|
| | **Initial** | **Case 1** | **Case 2** | **Initial** | **Case 1** | **Case 2** | **Initial** | **Case 1** | **Case 2** |
| $C_L$ | 0.500 | 0.500 | 0.500 | 0.500 | 0.500 | 0.500 | 0.500 | 0.500 | 0.500 |
| $C_D$ | 0.0212 | 0.0193 | 0.0192 | 0.0205 | 0.0191 | 0.0189 | 0.0681 | 0.0190 | 0.0189 |
| $\frac{C_L}{C_D}$ | 23.6 | 25.9 | 26.0 | 24.4 | 26.2 | 26.5 | 7.34 | 26.3 | 26.4 |
| $C_M$ | -0.1740 | -0.1700 | -0.2090 | -0.1628 | -0.1699 | -0.1927 | -0.0114 | -0.1695 | -0.1994 |
| $\alpha$ (°) | 2.32 | 2.70 | 1.93 | 2.41 | 2.48 | 2.28 | 5.40 | 2.49 | 2.01 |

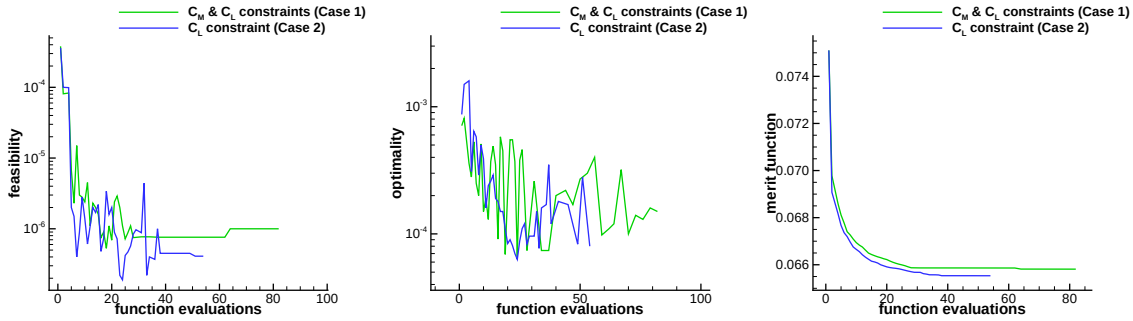


**a) feasibility** **b) optimality** **c) merit function**

**Fig. 3 Convergence histories of blunt trailing-edge CRM cases**

represents the ability of the optimizer to meet the nonlinear constraints, optimality is a measure of the gradient of SNOPT's Lagrangian merit function, and the merit function represents the objective function and any nonlinear constraint violations. In each case, the feasibility is improved by at least two orders of magnitude. Optimality is reduced by a maximum of one order of magnitude; deeper convergence is difficult to achieve without either reducing the number of design variables or imposing tighter constraints on them.

Contour plots of the coefficient of pressure are presented for the initial and optimized results from all three initial geometries in Figs. 6, 7, and 8. In the case of the wing with the blunt trailing edge, the results of Cases 1 and 2 have done a good job of removing the shocks present on the surface of the initial geometry. A spike in the coefficient of pressure is present near the leading edge of the initial geometry; this is caused by the fitting of the computational mesh, which is not able to perfectly capture the curvature of the leading edge. However, it is interesting to note that the optimizer is able to reduce this effect. The results of the optimizations of the sharp trailing-edge configuration and the geometry with NACA0012 sections are shock-free.

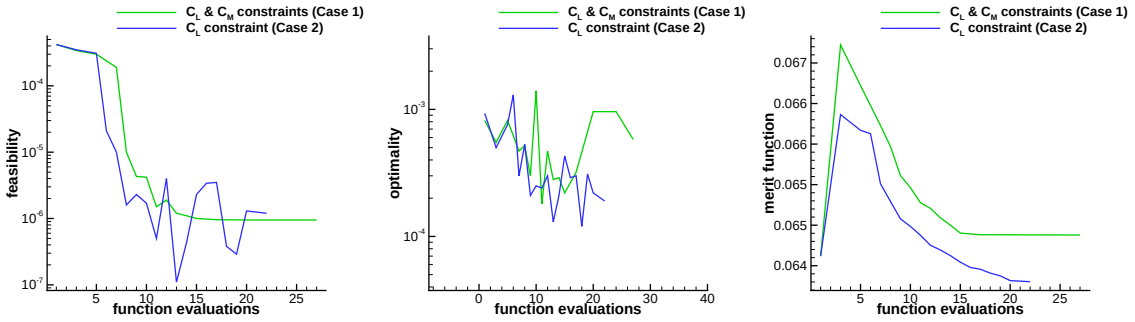


a) feasibility b) optimality c) merit function

**Fig. 4 Convergence histories of sharp trailing-edge CRM cases**

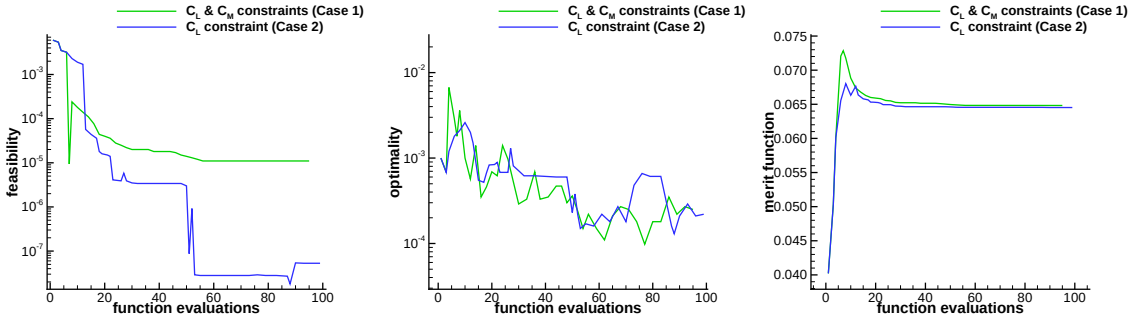


a) feasibility b) optimality c) merit function

**Fig. 5 Convergence histories of NACA0012 CRM cases**

The spanwise lift distributions of the initial geometry and the results of Cases 1 and 2 are compared to an elliptical distribution in Fig. 9 for each of the geometries considered. The optimized blunt trailing-edge cases show distributions much closer to elliptical than the distribution corresponding to the initial geometry. In the case of the sharp trailing edge, Case 2 was able to achieve a near-elliptical distribution, while the distribution resulting from Case 1 was not, although there is visible improvement compared to the initial geometry. For the initial geometry with NACA0012 sections, Case 2 is able to achieve a nearly elliptical distribution. Maintaining the pitching moment constraint in Case 1, however, may be preventing the optimizer from achieving the tip loading necessary to produce an overall elliptical distribution.

The optimization of the wing with NACA0012 sections applied to the initial CRM wing planform produces similar drag data at the target lift to those initialized with blunt and sharp trailing-edge CRM wing geometries, even though the optimizer appears to produce a different shape for each of the three geometries, particularly for the moment-constrained cases. The section geometries are

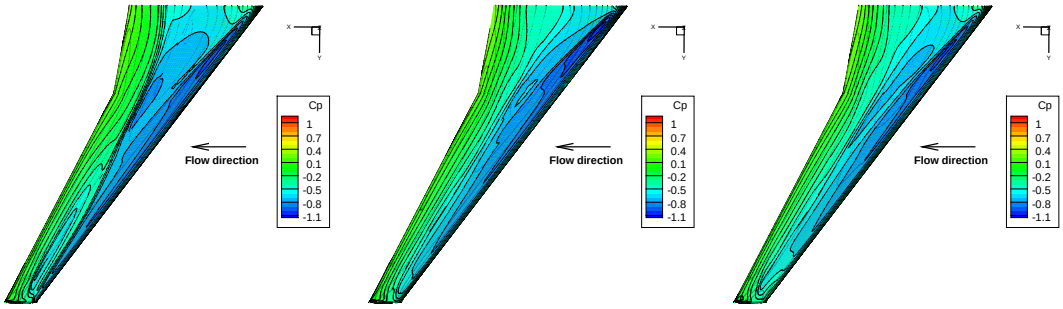


**a) Initial geometry** **b) $C_L$ and $C_M$ constraints** **c) $C_L$ constraint**

**Fig. 6 Surface pressure coefficient contours on the upper surface for the blunt trailing-edge CRM cases**

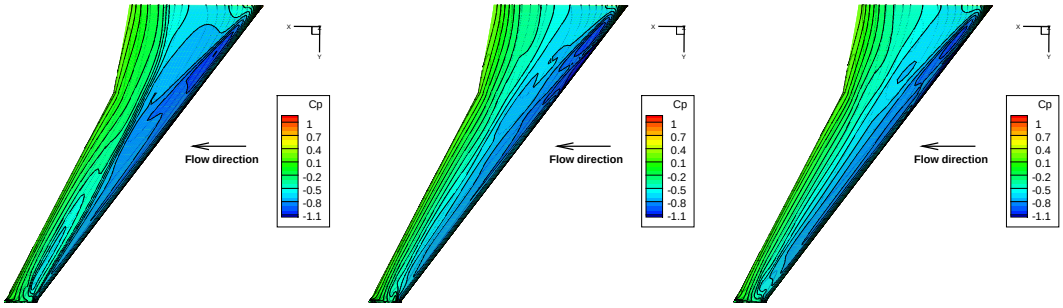


**a) Initial geometry** **b) $C_L$ and $C_M$ constraints** **c) $C_L$ constraintn**

**Fig. 7 Surface pressure coefficient contours on the upper surface for the sharp trailing-edge CRM cases**

compared for the cases using the lift and pitching moment constraints in Fig. 10 and for the cases with no moment constraint in Fig. 11. With the exception of the 2.35% span location, the blunt and sharp trailing-edge geometries appear to be producing similar results at the inboard sections. As the sections are observed further outboard, however, there is more similarity between the sharp trailing-edge and NACA0012-sectioned geometries. The fact that the NACA0012-sectioned wing was able to achieve the same lift and drag as the two CRM wings, despite starting from a very different initial geometry, while also producing a final geometry that differs substantially from the results of the sharp and blunt trailing-edge CRM wings, suggests that the design space for this problem is either multi-modal or contains a flat valley.

For the blunt trailing edge case shown in Fig. 10, the final geometry contains a sharp feature at the leading edge that is most noticeable near the wing tip. This feature is likely the result of the high degree of geometric flexibility at the leading edge, which the optimizer exploits to improve the load distribution while satisfying the pitching moment constraint. This effect is reduced when

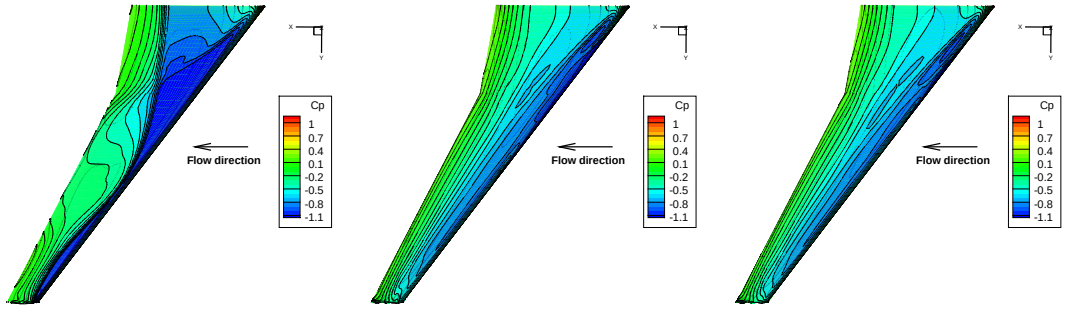


**a) Initial geometry** **b) $C_L$ and $C_M$ constraints** **c) $C_L$ constraint**

**Fig. 8 Surface pressure coefficient contours on the upper surface for the NACA0012 CRM cases**

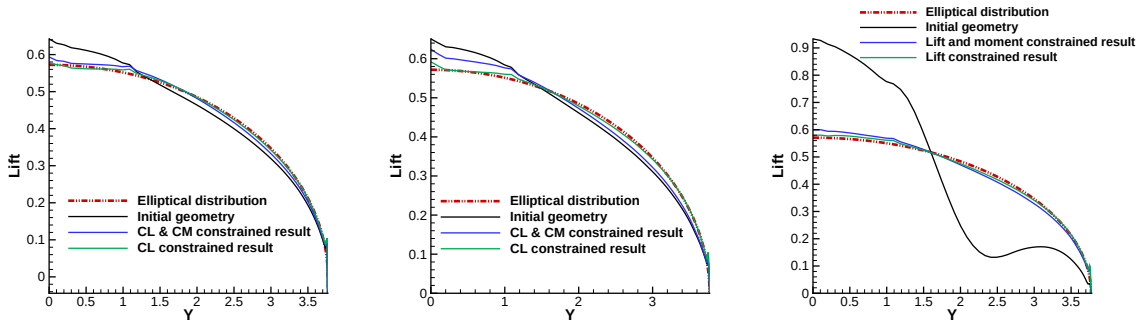


**a) Blunt TE** **b) Sharp TE** **c) NACA0012**

**Fig. 9 Lift distribution comparison for CRM wing optimizations**

multiple operating conditions are considered, and could be eliminated if dive constraints are used [14]. Introducing additional constraints limiting the geometric flexibility near the leading edge could also prevent this. Moreover, the optimized wings have thinner outboard sections with thicker sections near the wing root relative to the original CRM geometry. We emphasize that this is a test problem to characterize the performance of an aerodynamic shape optimization methodology, not a practical wing design study. A high degree of geometric flexibility has been permitted in order to provide a stiff test of the optimization methodology.

To obtain a better understanding of the nature of the design space for the CRM study, several different sets of perturbations were applied to the CRM planform wing with NACA0012 sections initially. The drag minimization with constrained lift and pitching moment was run for each of the new initial geometries. To create the modified geometries, the sharp trailing-edge CRM wing geometry is used initially; the $z$-coordinates of the CRM planform wing with NACA0012 sections are then applied to isolated sections of the initial geometry, creating a family of initial designs. The

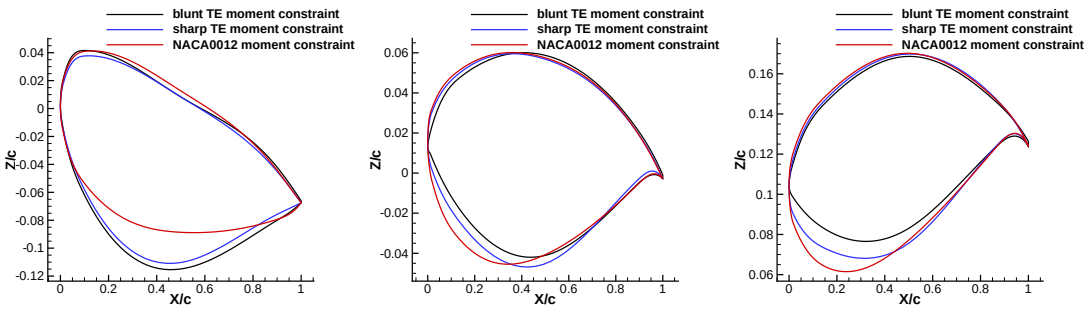


a) 2.35% span b) 26.7% span c) 55.7% span

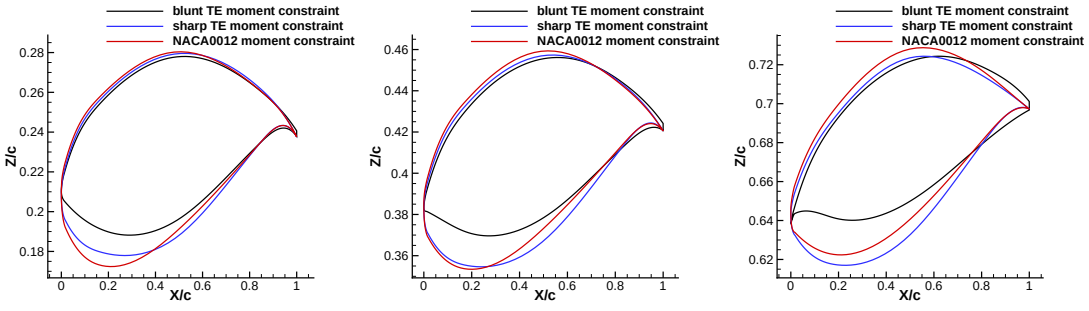


d) 69.5% span e) 82.8% span f) 94.4% span

**Fig. 10 Section shape comparison for three CRM wing geometries, drag objective with lift and moment constraints**

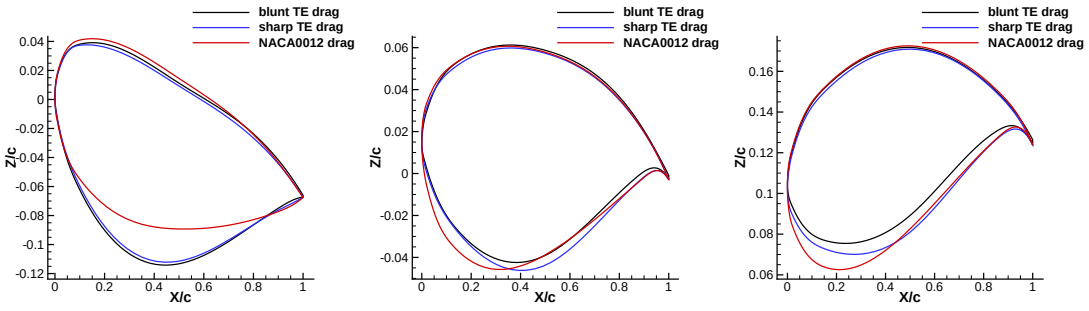


a) 2.35% span b) 26.7% span c) 55.7% span

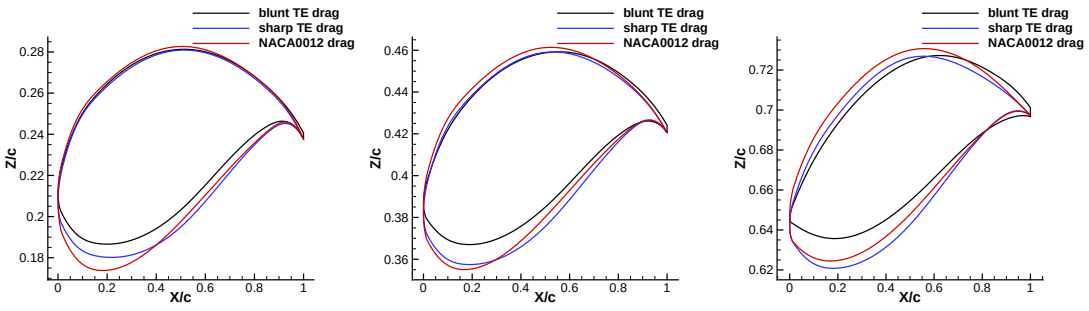


d) 69.5% span e) 82.8% span f) 94.4% span

**Fig. 11 Section shape comparison for three CRM wing geometries, drag objective with lift constraint**

**Table 5 Summary of initial geometries for CRM wing design space investigation**

| Initial Design # | NACA0012 Data Applied To: |
|---|---|
| 1 | Inboard patches only |
| 2 | Outboard patches only |
| 3 | Upper surface patches only |
| 4 | Lower surface patches only |
| 5 | Upper inboard patches only |
| 6 | Lower inboard patches only |
| 7 | Upper outboard patches only |
| 8 | Lower outboard patches only |

**Table 6 Coefficient data from design space study of CRM wing with sharp trailing edge**

| Initial Design # | $C_L$ | $C_D$ | $C_M$ |
|---|---|---|---|
| 1 | 0.500 | 0.0189 | -0.1698 |
| 2 | 0.500 | 0.0189 | -0.1700 |
| 3 | 0.500 | 0.0190 | -0.1698 |
| 4 | 0.500 | 0.0191 | -0.1699 |
| 5 | 0.497 | 0.0188 | -0.1685 |
| 6 | 0.500 | 0.0190 | -0.1699 |
| 7 | 0.500 | 0.0189 | -0.1700 |
| 8 | 0.500 | 0.0189 | -0.1698 |

initial designs are summarized in Table 5, which lists the regions of the initial geometry to which the NACA0012 data are applied. The section shapes of the set of initial geometries are shown in Fig. 12. The optimizer achieved at least one order reduction in optimality in each case. Despite the comparison of the eight final geometries in Fig. 13 showing that the optimizer produces visibly different results for the different initial geometries, each of the results exhibits comparable drag and pitching moment coefficients at the target lift coefficient, as shown in Table 6. This indicates that the design space for this problem is relatively flat and provides an explanation as to why the sharp trailing-edge CRM wing and the CRM planform wing with NACA0012 sections produced different geometries. However, the possibility of a multi-modal design space cannot be completely discounted; deeper convergence of the optimizer would allow for a more definitive conclusion as to whether the design space contains a flat valley or is multi-modal.

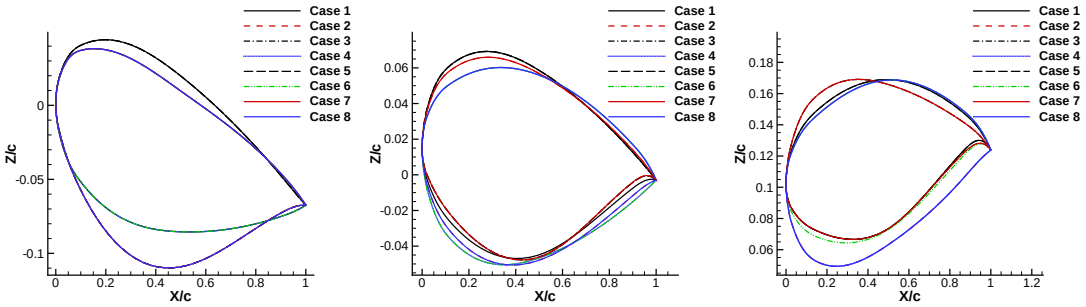


a) 2.35% span b) 26.7% span c) 55.7% span

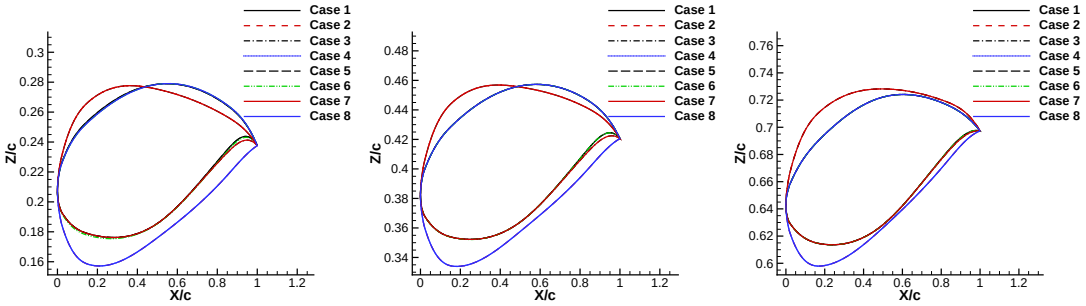


d) 69.5% span e) 82.8% span f) 94.4% span

**Fig. 12 Section shapes of initial geometries for multi-modality study of CRM wing**

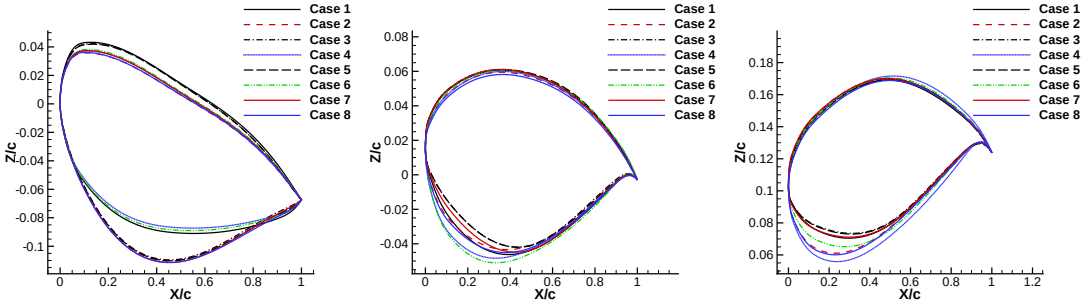


a) 2.35% span b) 26.7% span c) 55.7% span

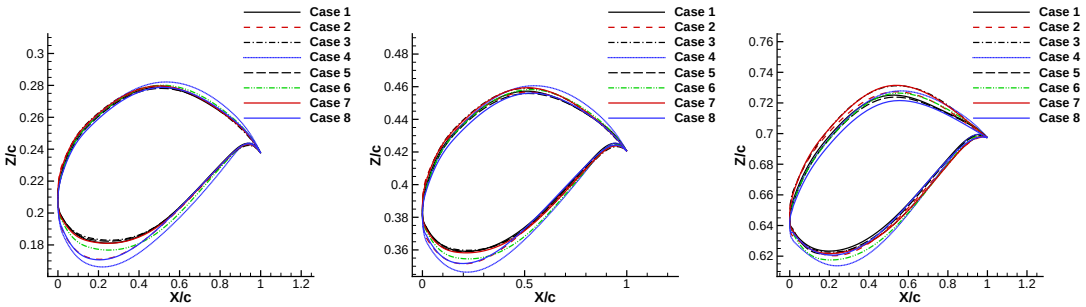


d) 69.5% span e) 82.8% span f) 94.4% span

**Fig. 13 Section shapes of final geometries for multi-modality study of CRM wing**

**Table 7 Coefficients for CRM wing with blunt trailing edge on optimization mesh and fine mesh**

| | Initial Geometry | | Optimized Geometry | |
|---|---|---|---|---|
| Mesh Size (nodes) | $3.4 \times 10^6$ | $39.8 \times 10^6$ | $3.4 \times 10^6$ | $39.8 \times 10^6$ |
| $C_L$ | 0.500 | 0.500 | 0.500 | 0.500 |
| $C_D$ | 0.0212 | 0.0197 | 0.0193 | 0.0186 |
| $C_M$ | -0.1740 | -0.1862 | -0.1700 | -0.1730 |

**Table 8 Coefficients for CRM wing with sharp trailing edge on optimization mesh and fine mesh**

| | Initial Geometry | | Optimized Geometry | |
|---|---|---|---|---|
| Mesh Size (nodes) | $11.0 \times 10^6$ | $35.5 \times 10^6$ | $11.0 \times 10^6$ | $35.5 \times 10^6$ |
| $C_L$ | 0.500 | 0.500 | 0.500 | 0.500 |
| $C_D$ | 0.0205 | 0.0203 | 0.0191 | 0.0188 |
| $C_M$ | -0.1628 | -0.1640 | -0.1699 | -0.1711 |

To ensure that the improvement in the drag coefficient carries over to a very fine grid level, the initial and optimized geometries were evaluated on meshes made up of over 35 million nodes in Tables 7, 8, and 9. The coefficients obtained on the fine mesh are compared to those obtained from the mesh used in the optimization with lift and pitching moment constraints. At the target lift coefficient, the largest discrepancy is in the drag coefficient for the initial blunt trailing-edge geometry, which exhibits a difference of 7.6% relative to the drag coefficient on the fine mesh. The pitching moment coefficient differs by 6.6% relative to the fine mesh. For the optimized blunt trailing-edge geometry, the drag coefficient and pitching moment coefficient differ by 3.8% and 0.02%, respectively, between the mesh used in the optimization and the fine mesh. A 5.6% relative improvement in drag is demonstrated on the fine mesh between the initial and final geometries. This demonstrates that the geometry produced by the optimizer significantly reduces the objective function relative to the original geometry, even on a finer mesh than that used for the optimization. Good agreement in the lift and pitching moment coefficients is also demonstrated between the coarser and fine meshes for the sharp trailing-edge and NACA0012 configurations. However, if strict satisfaction of a constraint such as the pitching moment is desired, then a finer mesh should be used for the optimization.

**Table 9 Coefficients for CRM wing with NACA0012 sections on optimization mesh and fine mesh**

| | **Initial Geometry** | | **Optimized Geometry** | |
|---|---|---|---|---|
| Mesh Size (nodes) | $11.0 \times 10^6$ | $35.5 \times 10^6$ | $11.0 \times 10^6$ | $35.5 \times 10^6$ |
| $C_L$ | 0.500 | 0.500 | 0.500 | 0.500 |
| $C_D$ | 0.0681 | 0.0611 | 0.0191 | 0.0190 |
| $C_M$ | -0.0114 | -0.0400 | -0.1700 | -0.1699 |

### B. Optimization with Section Shape and Planform Design Variables

Since structures are not considered in the cases presented in this paper, the wing planform shapes are typically fixed. However, the aerodynamic shape optimization algorithm will eventually be incorporated with a structural solver so that aerostructural optimization can be performed. Consequently, it is important to ensure that the aerodynamic optimization algorithm is capable of accommodating large planform changes as well as section shape changes. Here we present such an optimization problem. It is intended solely to demonstrate the ability of the methodology to handle large geometric changes such as can be encountered in an aerostructural optimization; it is not a practical example.

The initial geometry is a rectangular wing initially fit with NACA0012 sections. The root chord is used as the reference length. The initial wing has a semi-span of 2.0 reference units and a projected area of 2.0 squared reference units. The computational mesh is made up of 12 blocks and 8.46 million nodes; each block of the mesh is parameterized with a $9 \times 9 \times 9$ B-spline control volume. Flow analysis is performed on a 96-block equivalent mesh that is obtained by subdividing each block of the 12-block mesh into 8 blocks. The parameter extraction method is used to obtain an average off-wall spacing of $2.53 \times 10^{-6}$ reference units, resulting in an average $y^+$ value of 0.4.

The $z$-coordinates of the B-spline control points on the aerodynamic surface are used as section and twist variables, along with the angle of attack. The trailing-edge control points are fixed. Additionally, the leading-edge and trailing-edge sweep angles are allowed to vary, creating taper. The span can also increase. In total, this problem has 131 design variables. A minimum volume constraint is enforced based on the initial geometry. The sweep angles have an upper bound of 45.0°, while the semi-span has an upper bound of 5.0 reference units. We reiterate that the geometries produced in this study are not meant to represent practical aerodynamic configurations; rather, the

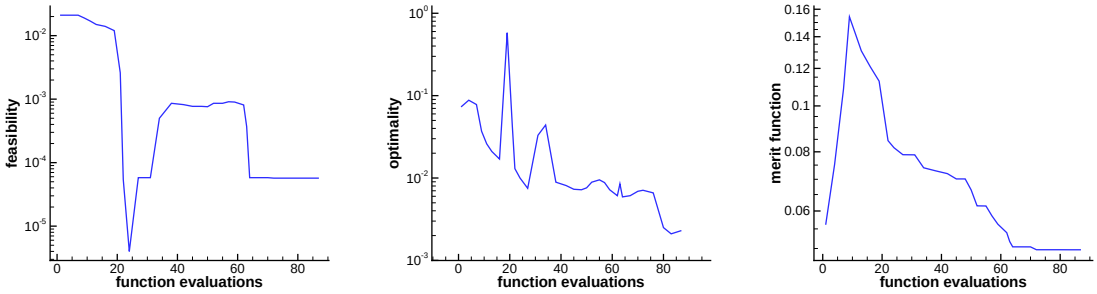


**a) Feasibility** **b) Optimality** **c) Merit function**

**Fig. 14 Convergence history for optimization of rectangular wing in transonic flow**

purpose of this study is to demonstrate the geometric flexibility and robustness of the presented methodology in the presence of large shape changes.

The objective of this design problem is to minimize drag at a Mach number of 0.84 and a Reynolds number of 5 million, subject to a lift constraint, where the constrained lift quantity is defined as the product of the lift coefficient and the reference area, $C_L * S_{\text{ref}}$. The projected area is used as the reference area. Note that the initial geometry cannot satisfy the $C_L * S_{\text{ref}}$ constraint.

Convergence data are presented in Fig. 14, where, after 120 hours on 108 processors, a reduction of between one and two orders of magnitude is observed in the optimality. The spikes in the convergence plots show where the optimizer must work to minimize the lift constraint penalty; after the lift approaches the target, the merit function decreases and eventually levels off. The lift and drag data corresponding to the initial and optimized geometries are compared in Table 10, where the coefficients corresponding to the initial geometry are obtained using the initial projected area of 2.0 squared reference units as the reference area, and the coefficients for the final geometry use the projected area of the final geometry, $S_{\text{ref}} = 3.7$ squared reference units. The data show that the lift-to-drag ratio has improved by a factor of four.

The changes in the planform variables are illustrated in Fig. 15, which shows a three-dimensional view of the initial and final surface geometries, with the positions of the B-spline control points represented as spheres. The wing is swept back and the span is increased by approximately 60% to 3.2 reference units. The minimum volume constraint is not active for the final geometry. The final leading-edge and trailing-edge sweep angles are 25.6° and 29.8°, respectively; neither angle reached

**Table 10 Lift, drag, and moment data for optimization of rectangular wing in transonic flow**

| | Initial geometry | Optimized geometry |
|---|---|---|
| $C_L * S_{\text{ref}}$ | 0.2888 | 0.9650 |
| $C_L$ | 0.1444 | 0.2594 |
| $C_D * S_{\text{ref}}$ | 0.0561 | 0.0472 |
| $C_D$ | 0.0280 | 0.0127 |
| $C_L/C_D$ | 5.1 | 20.4 |

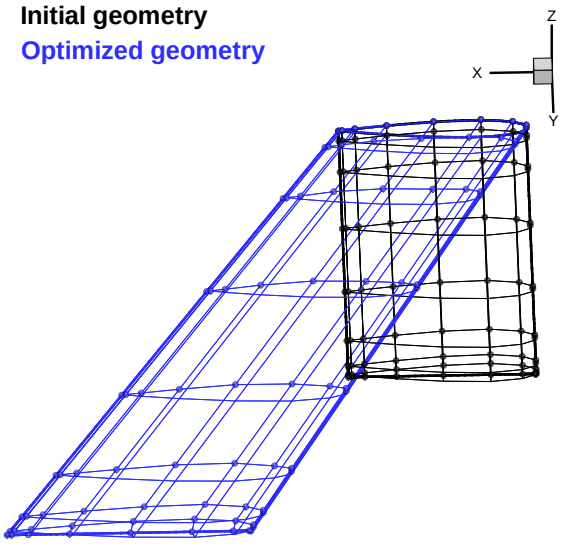


**Fig. 15 3D comparison of geometries from optimization of rectangular wing in transonic flow**

its upper bound of 45.0°, nor did the span reach its upper bound of 5.0 reference units. Section geometries at three spanwise stations, along with corresponding plots of coefficient of pressure, are presented in Figs. 16 and 17, respectively. Span percentages are specified relative to the initial geometry so that the locations of the sections (i.e. the $y$-coordinates corresponding to each spanwise section) remain consistent between the initial and optimized geometries. Additionally, noting the varying chord lengths along the span, the leading-edge coordinates are aligned in the images in order to facilitate a visual comparison. The coefficient of pressure data are obtained for the initial geometry at the initial lift coefficient of $C_L = 0.1444$ (where $S_{\text{ref}} = 2.0$ squared reference units) and the optimized geometry at the final lift coefficient, $C_L = 0.2594$ ($S_{\text{ref}} = 3.72$ squared reference units). The final geometry comprises thinner section shapes with a cambered trailing-edge, and the optimizer has significantly reduced the strength of the shock, although it was not able to eliminate

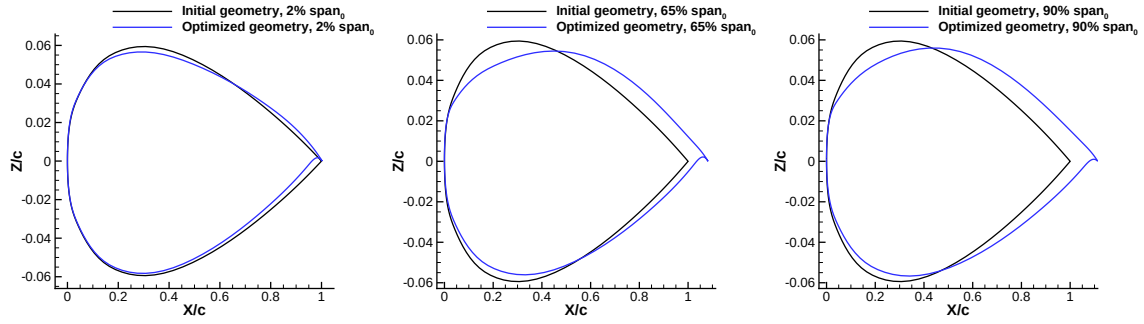


**Fig. 16 Section shapes for optimization of rectangular wing in transonic flow**

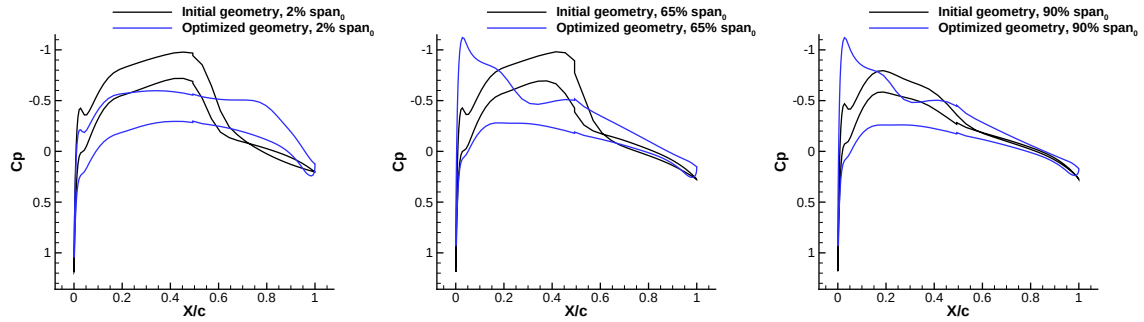


**Fig. 17 Surface pressure coefficient data for optimization of rectangular wing in transonic flow**

it entirely. The large improvement in lift-to-drag ratio results primarily from the reduction of wave drag from the near-elimination of shock waves and the induced drag reduction associated with the span increase.

The initial and final geometries were analyzed on a 30 million-node mesh, and the results are compared to the data obtained from the optimization on the 8.5 million-node mesh in Table 11. Although the force coefficients are not fully grid converged, the improvement in the lift-to-drag ratio is also seen on the fine mesh. Overall, this problem demonstrates the ability of the flow solver and mesh movement methodology to handle a wide variety of geometries. Thus, the optimization methodology is capable of addressing problems where large shape changes are encountered.

**Table 11 Coefficients for rectangular wing on optimization mesh and fine mesh**

| | Initial Geometry | | Optimized Geometry | |
|---|---|---|---|---|
| Mesh Size (nodes) | $8.5 \times 10^6$ | $30.2 \times 10^6$ | $8.5 \times 10^6$ | $30.2 \times 10^6$ |
| $C_L * S_{\text{ref}}$ | 0.2888 | 0.2888 | 0.9650 | 0.9650 |
| $C_L$ | 0.1444 | 0.1444 | 0.2594 | 0.2594 |
| $C_D * S_{\text{ref}}$ | 0.0561 | 0.0562 | 0.0472 | 0.0461 |
| $C_D$ | 0.0280 | 0.0281 | 0.0127 | 0.0124 |
| $C_L/C_D$ | 5.1 | 5.1 | 20.4 | 20.9 |

### C. Comparison of Optimization Based on the Euler Equations with that Based on the RANS Equations

Optimization based on inviscid analysis is a popular approach based on its low computational cost and high degree of robustness compared to viscous analysis. There are certainly situations in which a designer would be tempted to rely on inviscid analysis, and others in which viscous effects are too significant to ignore or approximate. For example, optimizations of high-lift, multi-element configurations, or geometries near their maximum lift, would require viscous analysis. However, in cases where the flow is fully attached and any shocks present are weak, inviscid analysis can predict lift and surface pressure distributions relatively accurately. In such cases, particularly within a multidisciplinary framework where the computational cost and potentially limited robustness associated with viscous analysis can be prohibitive, inviscid analysis is an attractive option. Approximations of the viscous drag can be obtained based on surface area.

To investigate the effect of relying on inviscid analysis in aerodynamic shape optimization, the drag minimization of the sharp trailing-edge CRM wing configuration with lift and pitching moment constraints presented in Section V A is repeated, this time based on the Euler equations. A RANS analysis is performed on the resulting geometry at the lift coefficient of $C_L = 0.50$ to compare the result of the optimization based on the Euler equations to that based on the RANS equations.

The section shapes produced by the Euler and RANS optimizations at six spanwise locations are presented in Fig. 18, followed by the corresponding distributions of coefficient of pressure based on a RANS computation in Fig. 19. While the geometry resulting from the RANS optimization is shock-free, a strong surface shock is present near the mid-chord for the Euler-optimized geometry. Note that, based on an inviscid analysis, the Euler-optimized geometry is shock-free; the shock arises

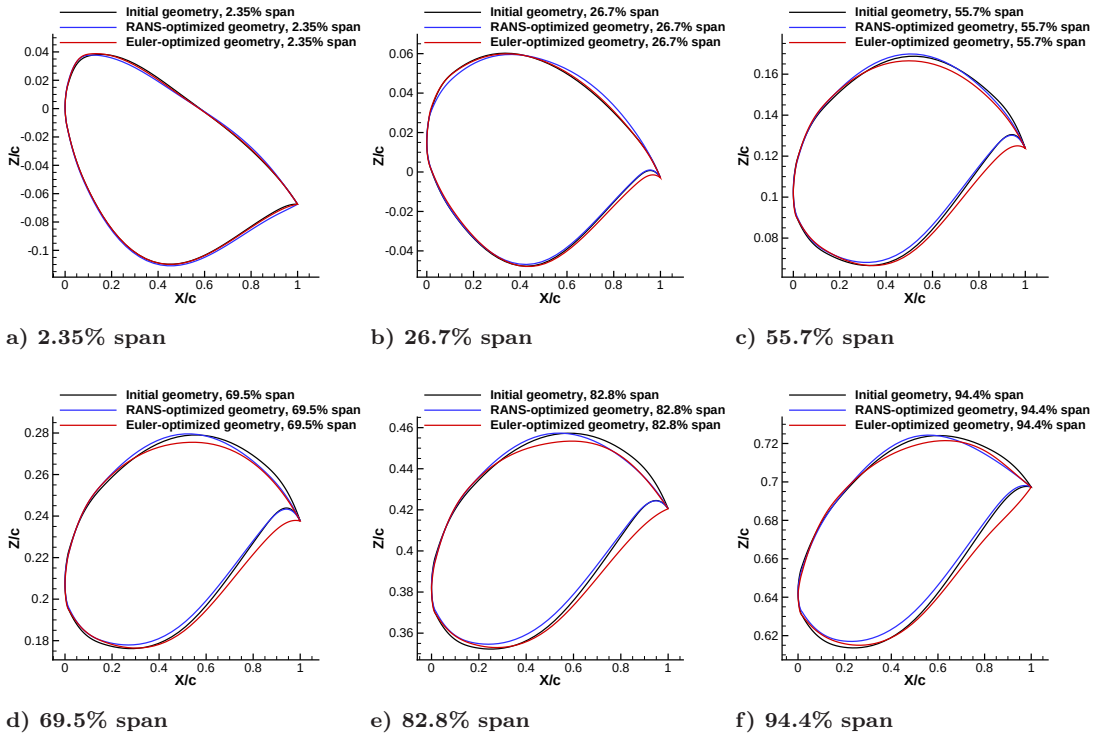


**a) 2.35% span** **b) 26.7% span** **c) 55.7% span**

**d) 69.5% span** **e) 82.8% span** **f) 94.4% span**

**Fig. 18 Comparison of section shapes from Euler and RANS optimizations of CRM wing with sharp trailing edge**

when the geometry is evaluated based on the RANS equations. In a similar case, flow separation was also observed near the trailing edge when an Euler-optimized geometry was analyzed based on the RANS equations [61].

The coefficients of lift, drag, and pitching moment corresponding to the optimizations based on the Euler and RANS equations are compared in Table 12. The RANS-optimized geometry produces a much lower drag coefficient compared to the geometry produced by the Euler optimization (reevaluated using the RANS equations). The Euler-based optimization produces a geometry that is inferior to both the RANS-based result and the initial geometry. There are three primary problems with Euler-based optimization, even under cruise conditions. First, shock elimination requires subtle modifications to the geometry in the vicinity of the shock. The addition of the boundary layer perturbs the flow sufficiently that the modifications produced by the Euler-based optimization are no longer appropriate. Second, the Euler-based optimization is not constrained by the possibility of turbulent boundary-layer separation. Hence it tends to produce geometries with steep adverse pressure gradients near the trailing edge which do not perform well in viscous flow. Third, the pitching

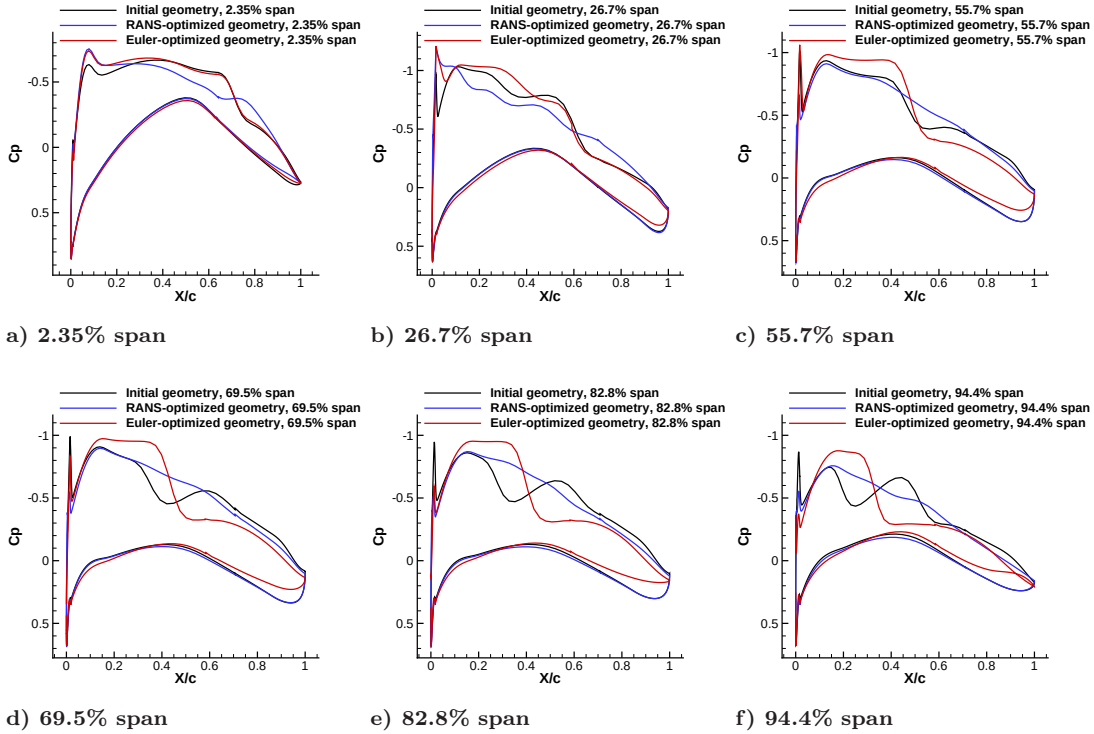


**a) 2.35% span** **b) 26.7% span** **c) 55.7% span**

**d) 69.5% span** **e) 82.8% span** **f) 94.4% span**

**Fig. 19 Comparison of surface pressure coefficient data from Euler and RANS optimizations of CRM wing with sharp trailing edge (RANS analysis)**

**Table 12 Force coefficient data from RANS analyses of Euler-based and RANS-based CRM optimizations with pitching moment constraint**

| Geometry | $C_L$ | $C_D$ | $C_M$ |
|---|---|---|---|
| **Initial** | 0.500 | 0.0205 | -0.1628 |
| **Euler result (RANS analysis)** | 0.500 | 0.0224 | -0.1260 |
| **RANS result** | 0.500 | 0.0191 | -0.1700 |

moment constraint is over-satisfied when the geometry optimized based on the Euler equations is analyzed based on the RANS equations.

### D. Wing-Fuselage-Tail Aircraft Optimization

A T-tail conventional aircraft configuration is considered for wing aerodynamic shape optimization in the presence of a fuselage and tail. The operating condition for a single-point optimization is at Mach number 0.82, $C_L = 0.513$, and Reynolds Number $19.1 \times 10^6$ based on wing mean-aerodynamic-chord. The design objective is to minimize the coefficient of drag subject to the following aerodynamic and geometric constraints. The optimized aircraft geometry must achieve a total lift corresponding to the aircraft weight. In addition to the total lift requirement, a prescribed

spanwise lift distribution is enforced on the wing as described in Section IV H. The lift distribution fixes the lift generated by the wing, while the fuselage and tail must generate the remaining lift to achieve the total lift constraint. Furthermore, it is critical that the wing location and its prescribed share of total lift be carefully specified to ensure optimal load balancing with respect to the fuselage and tail. A lower-fidelity conceptual design tool can be employed to achieve an aircraft configuration that reasonably satisfies this objective. The trim constraint, $C_M = 0$, is evaluated at the aircraft center of gravity. The region design variable approach described in Section IV F is used to handle geometric design variables and constraints. Geometric constraints are imposed on wing volume, sectional areas, and sectional thicknesses to ensure the wing outer mold line is sufficient to accommodate the internal wing structure and fuel volume. Sectional areas and wing volume are prevented from decreasing below their initial values. Local sectional thickness values cannot decrease by more that 25% of their initial values. The optimizer is only given the freedom to vary wing sectional shapes and twist while maintaining a fixed planform. In addition to the above geometric flexibility, wing, tail, and aircraft angle of attack are allowed to vary. The total number of design variables is 508. The initial wing geometry has a planform and lift distribution obtained from a medium-fidelity aerostructural optimization and uses RAE 2822 airfoil sections. The tail geometry is fixed.

The mesh used for the optimization has an average off-wall spacing of $2.5 \times 10^{-6}$ reference chords. The reference chord is the wing mean-aerodynamic-chord, which has a value of 12.8 feet. The blocking topology consists of $7.5 \times 10^6$ nodes partitioned over 620 blocks, each of size $23 \times 23 \times 23$ nodes. Figure 20 shows the aircraft geometry and illustrates the blocking topology.

At the end of the optimization, the performance of the optimized T-tail aircraft configuration does not change significantly between iterations, all constraints are satisfied, and optimality has been reduced by more than two orders of magnitude. Figure 21 shows the convergence history. Table 13 summarizes the aerodynamic performance of the initial and optimized T-tail configurations. The optimized wing geometry achieves a 27% reduction in $C_D$. To obtain a more accurate prediction of performance, the optimized geometry is analysed on a 24-million-node fine grid with the same blocking topology as the coarse grid used for optimization. At the target lift coefficient the value of $\frac{C_L}{C_D}$ obtained on the fine grid is 16.60. This result is not fully grid converged; the grid-converged lift

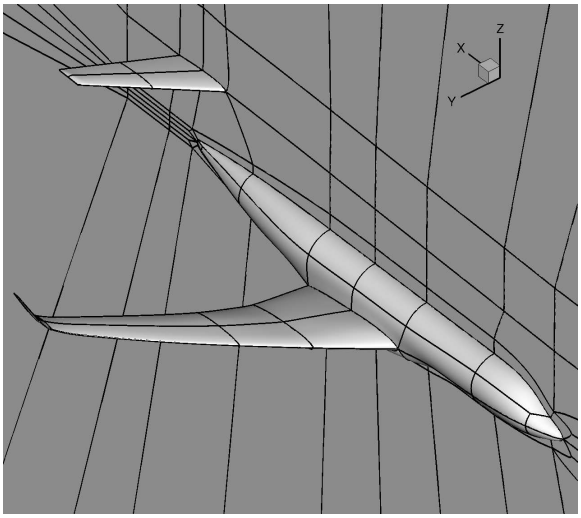


**Fig. 20 T-tail aircraft geometry and CFD mesh blocking topology**

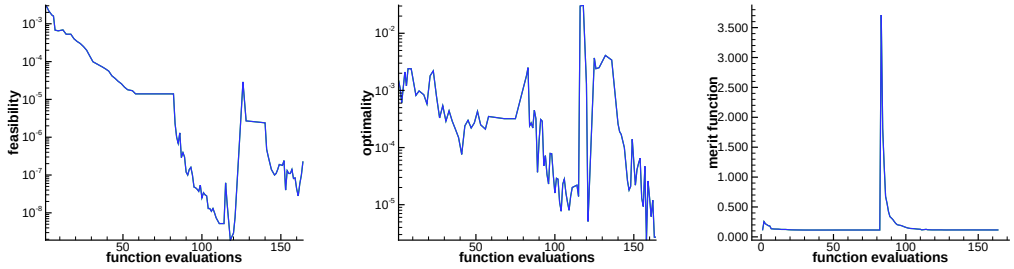


**a) feasibility** **b) optimality** **c) merit function**

**Fig. 21 Convergence history for the wing-body-tail optimization case**

to drag ratio is likely somewhat higher. Figure 22 shows that the spanwise lift distribution of the optimized wing matches the prescribed lift distribution. A comparison of pressure distributions and sections at spanwise locations on the initial and optimized wings is shown in Fig. 23. The optimized wing geometry eliminates the shock at mid-span that is evident on the initial wing geometry. These results demonstrate the capability of the aerodynamic shape optimization methodology to design a wing for minimum drag at turbulent, transonic operating conditions for a trimmed T-tail aircraft configuration by eliminating shocks on the wing while maintaining a prescribed lift distribution.

### E. Blended Wing-Body Optimization

The blended wing-body (BWB) aircraft concept has the potential to offer significant fuel-burn reductions compared to conventional transport aircraft. We demonstrate the optimization algorithm

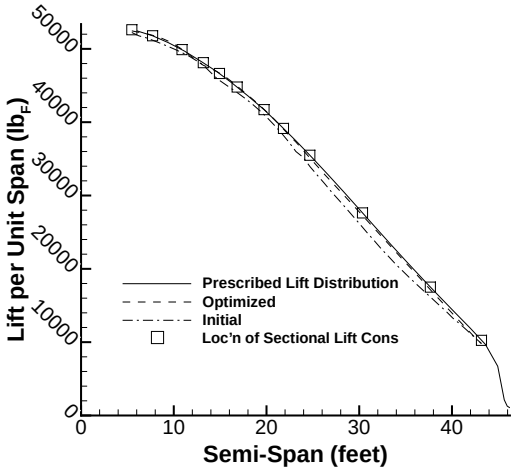


**Fig. 22 Spanwise lift distributions of initial and optimized wings compared to prescribed lift distribution**

| | | | Optimized |
|---|---|---|---|
| | Baseline | Optimized | (Fine Grid Analysis) |
| $C_L$ | 0.513 | 0.513 | 0.513 |
| $C_D$ | 0.0507 | 0.0369 | 0.0309 |
| $\frac{C_L}{C_D}$ | 10.12 | 13.89 | 16.60 |
| $C_M$ | 0.000 | 0.000 | 0.000 |
| $\alpha$ (°) | 3.04 | 1.86 | 1.87 |

**Table 13 Performance for initial and optimized T-tail aircraft geometries. Aircraft Mach number 0.82, Reynolds number** $19.1 \times 10^6$**.**

on the optimization of a 100-passenger regional jet for a 500nmi mission. Details of the baseline BWB design can be found in Reist and Zingg [72].

A single-point drag minimization optimization is performed for a 500nmi mission with the aircraft cruising at Mach 0.80 and 40,000ft. This leads to a Reynolds number based on the mean aerodynamic chord of $62\times10^6$. For the optimization, a 3.9 million node, 168 block grid is used with an off-wall spacing of $y^+ \approx 1.0$ at cruise. The baseline and optimized designs are analyzed on a family of refined grids with up to 32 million nodes with a minimum average off-wall spacing of $y^+ \approx 0.25$.

The CFD surface and its parametric representation are shown in Fig. 24a). In the absence of a structural model, trade-offs between aerodynamic performance and structural weight resulting from planform changes are not captured, thus the planform is held constant during the optimization, and the geometric design variables consist of the twist and section shapes over the entire aircraft.

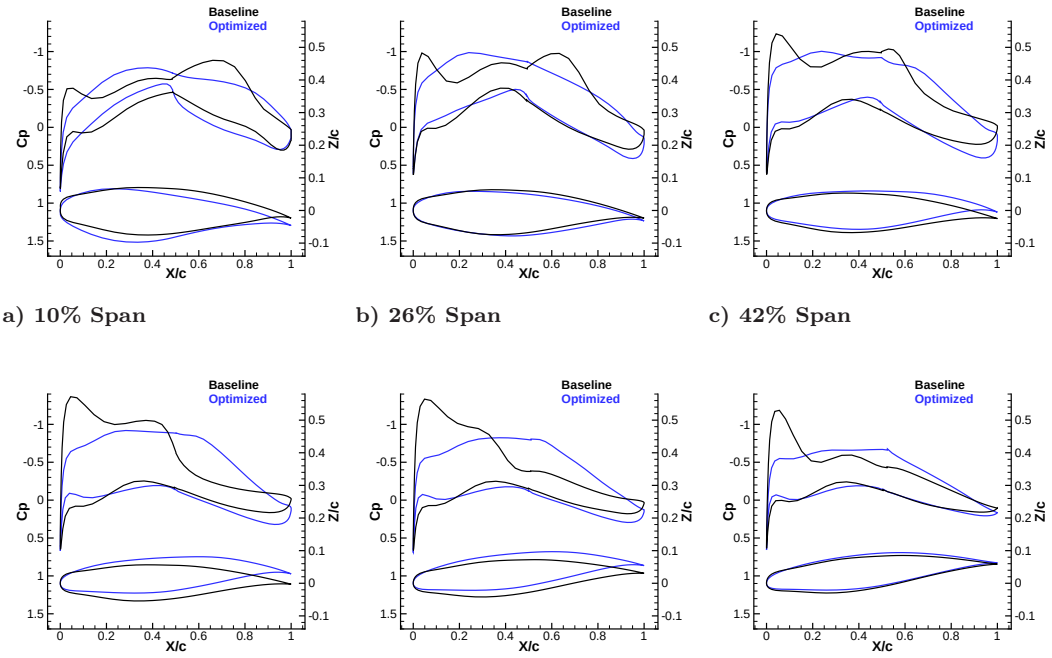


**a) 10% Span** **b) 26% Span** **c) 42% Span**

**d) 58% Span** **e) 74% Span** **f) 90% Span**

**Fig. 23 T-tail aircraft wing sections and pressure distributions for initial and optimized geometries**

In addition, the angle-of-attack of the aircraft is a design variable and is constrained to be within $\pm 3.0°$ such that the deck angle at cruise does not inhibit cabin operations. In order to maintain the required space for a passenger compartment, a polyhedron representing the passenger compartment, shown in Fig. 24b), forms a constraint such that the outer mold line cannot encroach upon the cabin. In addition, the wing volume is constrained such that the required 4500gal fuel volume can fit within 80% of the wing outer mold line volume. The $t/c$ of the sections over the entire aircraft are prevented from decreasing by more than 25% of their initial value. In total there are 495 design variables. Finally, the aircraft must be trimmed, that is at cruise $C_L = \frac{W}{q_\infty S} = 0.23$ and $C_M = 0$ about the center of gravity.

An Euler-based optimization is first performed in order to eliminate shocks in the inviscid design space and obtain a more suitable starting point for the RANS-based optimization. While the Euler optimized design is shock free, when analyzed with RANS the shocks return, but are weaker than on the unoptimized baseline. From here on, "the baseline" shall refer to the Euler-optimized design from which the RANS-based optimization is started. The optimization convergence history for the

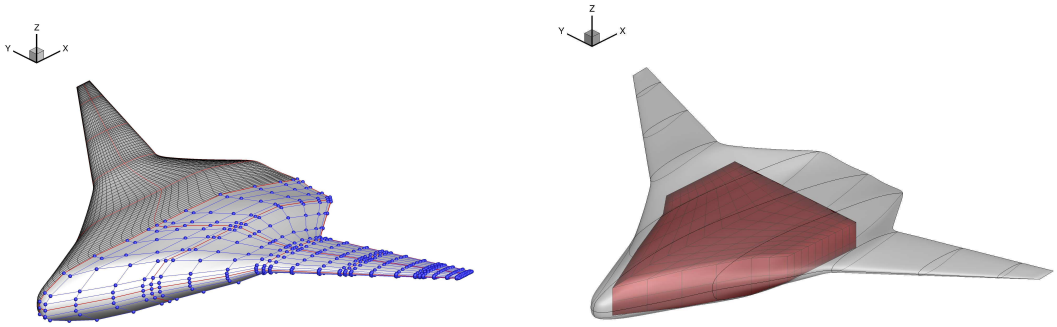

a) Baseline BWB surface grids. B-spline control points are shown as blue spheres

b) Polyhedron forming the cabin shape constraint

**Fig. 24 The baseline BWB design**

RANS-based optimization is shown in Fig. 25. At the end of the optimization the reduction in the objective between iterations is insignificant, all constraints are satisfied, and the optimality has been reduced by one order of magnitude. A 13.8% drag reduction is achieved over the baseline design, as shown in Table 14. Most of this drag reduction comes from the elimination of the shock as well as the reduction of separated flow, both of which are evident from the sectional pressure distributions shown in Fig. 26. The shock on the baseline is evident from 50% of the span outboard, as is its absence on the optimized design. While the initial Euler-based optimization achieved an elliptic lift-distribution on the wing in the Euler design space, this is lost in the RANS space, as seen in Fig. 27, due to the change in sectional loading caused by the reemergence of shocks and the introduction of separation in the RANS solution. The lift distribution resulting from the RANS-based optimization becomes more elliptical on the wing, but does not become perfectly elliptical. The imposition of the cabin shape and trim constraint affect the load-carrying capacity of the centerbody, which causes a deviation from the elliptical distribution. In addition, one would not expect a perfectly elliptical spanload, which is a result of linear aerodynamics, in the RANS-based optimization of a full-configuration for which the lifting surface is responsible for trim and whose planform has significant sweep and chord changes, essentially leading to a nonplanar wake.

A grid convergence study is performed on both the baseline and optimized designs with a three-member grid family of 8, 16, and 32 million node grids. The angle-of-attack is varied for each grid to achieve the target lift. The pitching moment target is satisfied during the optimization, but is not satisfied when the design is analyzed on the fine mesh. The results on both the finest

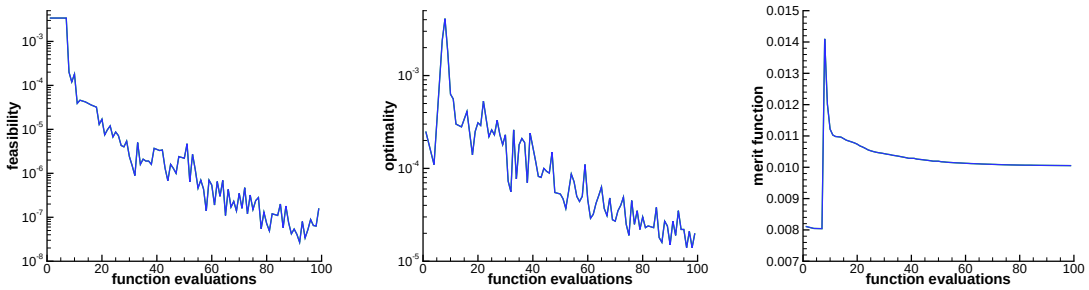


a) feasibility b) optimality c) merit function

**Fig. 25 Convergence histories of the BWB optimization case**

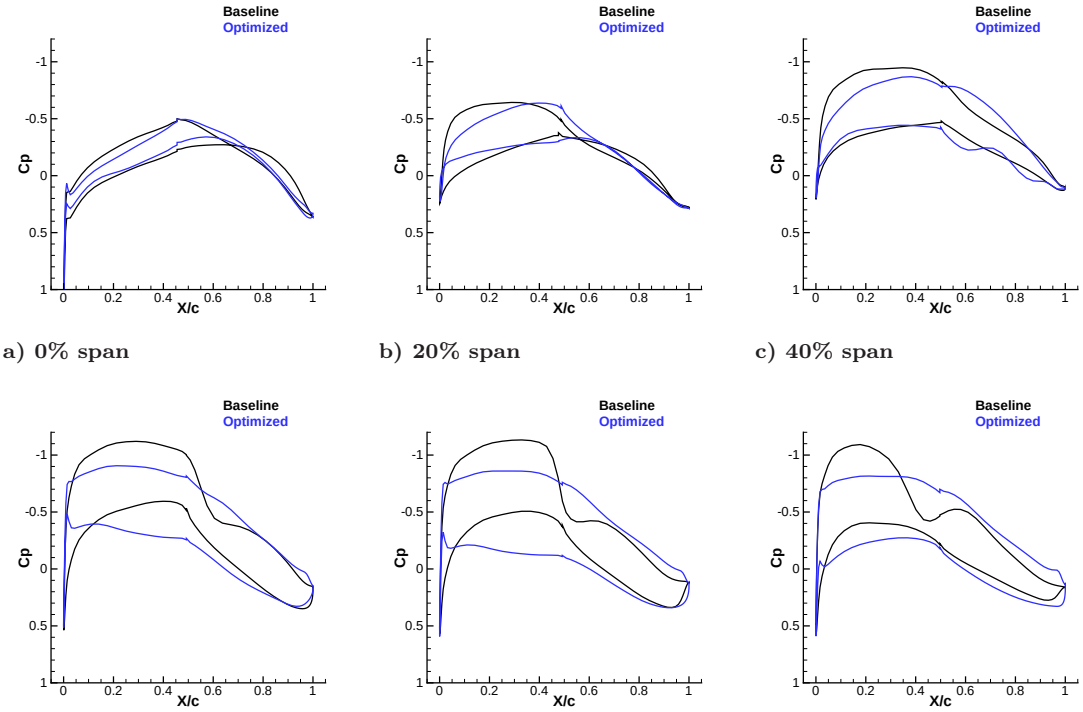


a) 0% span b) 20% span c) 40% span

d) 60% span e) 80% span f) 95% span

**Fig. 26 Coefficient of pressure distributions for the BWB case**

grid and the continuum value estimated from Richardson extrapolation ($\bullet^*$) are shown in Table 14. The 32 million node grid provides drag error of 2-3 counts for both designs when compared to the extrapolated continuum values. This optimization problem has demonstrated the applicability of the proposed algorithm for large-scale, high-speed, unconventional aircraft optimization problems.

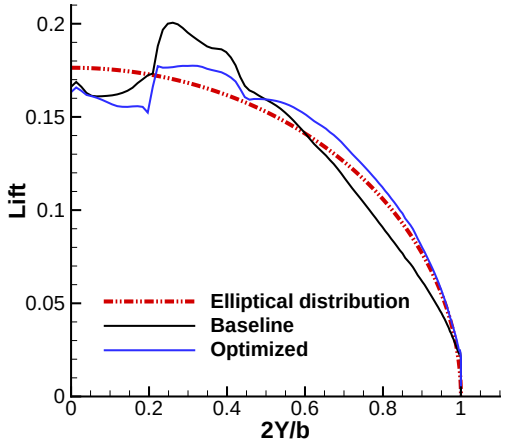


**Fig. 27 Lift distributions of the baseline and optimized BWB**

| | Baseline | Optimized |
|---|---|---|
| $C_L$ | 0.230 | 0.230 |
| $C_D$ | 0.0135 | 0.0118 |
| $C_D^*$ | 0.0132 | 0.0116 |
| $\frac{C_L}{C_D^*}$ | 17.4 | 19.8 |
| $C_M$ | 0.0234 | -0.0090 |
| $\alpha$ (°) | 4.65 | 2.40 |

**Table 14 Performance of the baseline and optimized BWB designs. Continuum values are indicated with an asterisk, while remaining values are presented for the finest grid level.**

## VI. Conclusions

A methodology is presented for performing high-fidelity aerodynamic shape optimization in steady turbulent flows. The integrated geometry parameterization and mesh movement methodology is based on B-spline tensor volumes and produces a subset of B-spline control points on the surface of the geometry that are used as design variables. High-fidelity numerical analysis based on the three-dimensional RANS equations is performed using a parallel Newton-Krylov-Schur flow solver. Constrained gradient-based optimization is carried out using SNOPT. The discrete-adjoint gradient evaluation was developed by hand and treats the turbulence model in a fully coupled manner. The evaluation includes a full hand linearization of the shock sensor.

Examples are presented to demonstrate the performance of the methodology for various aerodynamic configurations in turbulent flow conditions, including conventional wing geometries, a wing-body-tail configuration, and a blended wing-body configuration. The results show that geometries produced in optimizations based on inviscid flow analysis are inferior to designs obtained based on

viscous analysis. A spanwise lift distribution constraint is imposed for the wing-body-tail configuration. With this approach, the aerodynamic shape optimization reduces wave drag while having a minimal effect on wing structure and hence its weight. The methodology is also shown to be capable of robustly accommodating large changes in the geometry. Therefore the algorithm presented can be used in the context of detailed design, exploratory aerodynamic shape optimization, or as the aerodynamic module in a multidisciplinary optimization framework.

## Acknowledgments

The authors gratefully acknowledge financial assistance from the Natural Sciences and Engineering Research Council (NSERC), the Ontario Graduate Scholarship program, the Canada Research Chairs program, Bombardier Aerospace, and the University of Toronto.

Computations were performed on the GPC supercomputer at the SciNet HPC Consortium, part of Compute Canada.

## References

[1] "Boeing 787 Dreamliner provides new solutions for airlines, passengers," Tech. rep., Boeing, Seattle, WA, USA, 2013.

[2] "A350 XWB: Shaping efficiency," Tech. rep., Airbus, Toulouse, France, 2013.

[3] "X-48 Research: All good things must come to an end," Tech. rep., NASA, Edwards, CA, USA, 2013.

[4] Reist, T. A. and Zingg, D. W., "Aerodynamic shape optimization of a Blended-Wing-Body regional transport for a short range mission," *31st AIAA Applied Aerodynamics Conference*, AIAA–2013–2414, San Diego, CA, USA, June 2013.

[5] Drela, M., "Simultaneous optimization of the airframe, powerplant, and operation of transport aircraft," *In RAeS 2nd Aircraft Structural Design Conference, Hamilton Place, London*, 2010.

[6] Rogers, M. M., "Technical challenges to reducing subsonic transport drag," *50th AIAA Aerospace Sciences Meeting*, Nashville, TN, USA, Jan. 2012, http://ntrs.nasa.gov/search.jsp?R=20120006660.

[7] Gallman, J. W. and Kroo, I. M., "Structural optimization for joined-wing synthesis," *Journal of Aircraft*, Vol. 33, No. 1, 1996, pp. 214–223.

[8] Hicks, R. M. and Henne, P. A., "Wing design by numerical optimization," *Journal of Aircraft*, Vol. 15, No. 7, July 1978, pp. 407–412.

[9] Pironneau, O., "On optimum design in fluid mechanics," *Journal of Fluid Mechanics*, Vol. 64, No. 1, 1974, pp. 97–110.

[10] Jameson, A., "Aerodynamic design via control theory," *Journal of Scientific Computing*, Vol. 3, No. 3, 1988, pp. 233–260.

[11] Anderson, W. K. and Bonhaus, D. L., "Airfoil design on unstructured grids for turbulent flows," *AIAA Journal*, Vol. 37, No. 2, Feb. 1999, pp. 185–191.

[12] Nemec, M. and Zingg, D. W., "Newton-Krylov algorithm for aerodynamic design using the Navier-Stokes equations," *AIAA Journal*, Vol. 40, No. 6, 2002, pp. 1146–1154.

[13] Nemec, M., Zingg, D. W., and Pulliam, T. H., "Multipoint and multi-objective aerodynamic shape optimization," *AIAA Journal*, Vol. 42, No. 6, 2004, pp. 1057–1065.

[14] Buckley, H. P. and Zingg, D. W., "An approach to aerodynamic design through numerical optimization," *AIAA Journal*, Vol. 51, No. 8, 2013, pp. 1972–1981.

[15] Driver, J. and Zingg, D. W., "Numerical aerodynamic optimization incorporating laminar-turbulent transition prediction," *AIAA Journal*, Vol. 45, No. 8, Aug. 2007, pp. 1810–1818.

[16] Hicken, J. and Zingg, D., "Induced drag minimization of nonplanar geometries based on the Euler equations," *AIAA Journal*, Vol. 48, No. 11, 2010, pp. 2564–2575.

[17] Elliott, J. and Peraire, J., "Aerodynamic optimization on unstructured meshes with viscous effects," *13th AIAA Computational Fluid Dynamics Conference*, AIAA–97–1849, Snowmass, Colorado, June 1997.

[18] Elliott, J. K., *Aerodynamic optimization based on the Euler and Navier-Stokes equations using unstructured grids*, Ph.D. thesis, Massachusetts Institute of Technology, Cambridge, Massachusetts, USA, 1998.

[19] Jameson, A., Martinelli, L., and Pierce, N. A., "Optimum aerodynamic design using the Navier-Stokes equations," *Theoretical and Computational Fluid Dynamics*, Vol. 10, 1998, pp. 213–237.

[20] Nielsen, E. J. and Anderson, W. K., "Aerodynamic design optimization on unstructured meshes using the Navier-Stokes equations," *AIAA Journal*, Vol. 37, No. 11, Nov. 1999, pp. 1411–1419.

[21] Brezillon, J., Brodersen, O., Dwight, R., Ronzheimer, A., and Wild, J., "Development and application of a flexible and efficient environment for aerodynamic shape optimisation," *Proceedings of the ONERA-DLR Aerospace Symposium (ODAS), Toulouse*, 2006.

[22] Brezillon, J. and Dwight, R. P., "Applications of a discrete viscous adjoint method for aerodynamic shape optimisation of 3D configurations," *CEAS Aeronautical Journal*, Vol. 3, No. 1, 2012, pp. 25–34.

[23] Epstein, B., Jameson, A., Peigin, S., Roman, D., Harrison, N., and Vassberg, J., "Comparative study

of 3D wing drag minimization by different optimization techniques," *46th AIAA Aerospace Sciences Meeting and Exhibit*, AIAA–2008–326, Reno, Nevada, Jan. 2008.

[24] Sobieszczanski-Sobieski, J. and Haftka, R. T., "Multidisciplinary aerospace design optimization: survey of recent developments," *Structural optimization*, Vol. 14, No. 1, 1997, pp. 1–23.

[25] Alexandrov, N. M. and Hussaini, M. Y., *Multidisciplinary design optimization: State of the art*, Vol. 80, SIAM, 1997.

[26] Leoviriyakit, K., Kim, S., and Jameson, A., "Aero-structural wing planform optimization using the Navier-Stokes equations," *10th AIAA/ISSMO Multidisciplinary Analysis and Optimization Conference*, AIAA–2004–4479, Albany, New York, Aug. 2004.

[27] Martins, J. R. R. A., Alonso, J. J., and Reuther, J. J., "High-fidelity aerostructural design optimization of a supersonic business jet," *Journal of Aircraft*, Vol. 41, No. 3, May 2004, pp. 863–873.

[28] Kenway, G. K. W. and Martins, J. R. R. A., "Multi-point high-fidelity aerostructural optimization of a transport aircraft configuration," *Journal of Aircraft*, 2014, (In press).

[29] Kenway, G. K. W., Kennedy, G. J., and Martins, J. R. R. A., "A scalable parallel approach for high-fidelity steady-state aeroelastic analysis and derivative computations," *AIAA Journal*, 2014, (In press).

[30] Barcelos, M. and Maute, K., "Aeroelastic design optimization for laminar and turbulent flows," *Computer Methods in Applied Mechanics and Engineering*, Vol. 197, No. 19–20, 2013, pp. 1813–1832.

[31] Ghazlane, I., Carrier, G., Dumont, A., and Désidéri, J., "Aerostructural adjoint method for flexible wing optimization," *53rd AIAA/ASME/ASCE/AHS/ASC Structures, Structural Dynamics, and Materials Conference*, AIAA–2012–1924, Honolulu, HI, April 2012.

[32] Brezillon, J., Ronzheimer, A., Haar, D., Abu-Zurayk, M., Lummer, K., Krugër, W., and Nattere, F. J., "Development and application of multi-disciplinary optimization capabilities based on high-fidelity methods," *53rd AIAA/ASME/ASCE/AHS/ASC Structures, Structural Dynamics, and Materials Conference*, AIAA–2012–1757, Honolulu, HI, April 2012.

[33] Kulfan, B. M., "A universal parametric geometry representation method — "CST"," *The 45th AIAA Aerospace Sciences Meeting and Exhibit*, AIAA–2007–0062, Reno, Nevada, 2007.

[34] Mohammadi, B., "A new optimal shape design procedure for inviscid and viscous turbulent flows," *International Journal for Numerical Methods in Fluids*, Vol. 25, No. 2, July 1997, pp. 183–203.

[35] Nemec, M. and Aftosmis, M. J., "Aerodynamic shape optimization using a Cartesian adjoint method and CAD geometry," *24th AIAA Applied Aerodynamics Conference*, AIAA–2006–3456, San Francisco, California, United States, June 2006.

[36] Sederberg, T. W. and Parry, S. R., "Free-form deformation of solid geometric models," *SIGGRAPH*

*'86: Proceedings of the 13th annual conference on Computer graphics and interactive techniques*, ACM, New York, NY, USA, 1986, pp. 151–160.

[37] Gagnon, H. and Zingg, D. W., "Geometry generation of complex unconventional aircraft with application to high-fidelity aerodynamic shape optimization," *21st AIAA Computational Fluid Dynamics Conference*, AIAA–2013–2850, San Diego, CA, United Sates, June 2013.

[38] Anderson, W. K., Karman, S. L., and Burdyshaw, C., "Geometry parameterization method for multidisciplinary applications," *AIAA Journal*, Vol. 47, No. 6, 2009, pp. 1568–1578.

[39] Burgreen, G. W. and Baysal, O., "Three-dimensional aerodynamic shape optimization using discrete sensitivity analysis," *AIAA Journal*, Vol. 34, No. 9, Sept. 1996, pp. 1761–1770.

[40] Osusky, L. and Zingg, D. W., "Application of an efficient Newton-Krylov algorithm for aerodynamic shape optimization based on the Reynolds-averaged Navier-Stokes equations," *21st AIAA Computational Fluid Dynamics Conference*, AIAA–2013–2584, San Diego, CA, United States, June 2013.

[41] Lépine, J., Guilbault, F., Trépanier, J.-Y., and Pépin, F., "Optimized nonuniform rational B-spline geometrical representation for aerodynamic design of wings," *AIAA Journal*, Vol. 39, No. 11, Nov. 2001, pp. 2033–2041.

[42] Hicken, J. E. and Zingg, D. W., "Aerodynamic optimization algorithm with integrated geometry parameterization and mesh movement," *AIAA Journal*, Vol. 48, No. 2, Feb. 2010, pp. 400–413.

[43] Rogers, D. F. and Adams, J. A., *Mathematical Elements for Computer Graphics*, McGraw–Hill, Inc., New York, NY, 1990.

[44] Truong, A. H., Oldfield, C. A., and Zingg, D. W., "Mesh movement for a discrete-adjoint Newton-Krylov algorithm for aerodynamic optimization," *AIAA Journal*, Vol. 46, No. 7, July 2008, pp. 1695–1704.

[45] Meijerink, J. A. and van der Vorst, H. A., "An iterative solution method for linear systems of which the coefficient matrix is a symmetric M-matrix," *Mathematics of Computation*, Vol. 31, No. 137, Jan. 1977, pp. 148–162.

[46] Hicken, J. E. and Zingg, D. W., "A parallel Newton-Krylov solver for the Euler equations discretized using simultaneous approximation terms," *AIAA Journal*, Vol. 46, No. 11, Nov. 2008, pp. 2773–2786.

[47] Osusky, M. and Zingg, D. W., "Parallel Newton-Krylov-Schur flow solver for the Navier-Stokes equations discretized using summation-by-parts operators," *AIAA Journal*, Vol. 51, No. 12, 2013, pp. 2833–2851.

[48] Pulliam, T. H. and Zingg, D. W., *Fundamental Algorithms in Computational Fluid Dynamics*, Springer, 2014.

[49] Carpenter, M. H., Gottlieb, D., and Abarbanel, S., "Time-stable boundary conditions for finite-difference schemes solving hyperbolic systems: methodology and application to high-order compact

schemes," *Journal of Computational Physics*, Vol. 111, No. 2, 1994, pp. 220–236.

[50] Hesthaven, J. S., "A stable penalty method for the compressible Navier-Stokes equations: III. Multidimensional domain decomposition schemes," *SIAM Journal on Scientific Computing*, Vol. 20, No. 1, 1998, pp. 62–93.

[51] Carpenter, M. H., Nordström, J., and Gottlieb, D., "A stable and conservative interface treatment of arbitrary spatial accuracy," *Journal of Computational Physics*, Vol. 148, No. 2, 1999, pp. 341–365.

[52] Nordström, J. and Carpenter, M. H., "High-order finite difference methods, multidimensional linear problems, and curvilinear coordinates," *Journal of Computational Physics*, Vol. 173, No. 1, 2001, pp. 149–174.

[53] Osusky, M. and Zingg, D. W., "A parallel Newton-Krylov-Schur flow solver for the Navier-Stokes equations using the SBP-SAT approach," *50th AIAA Aerospace Sciences Meeting*, AIAA–2012–0442, Nashville, TN, United States, Jan. 2012.

[54] Svärd, M., Carpenter, M. H., and Nordström, J., "A stable high-order finite difference scheme for the compressible Navier-Stokes equations, far-field boundary conditions," *Journal of Computational Physics*, Vol. 225, No. 1, July 2007, pp. 1020–1038.

[55] Svärd, M. and Nordström, J., "A stable high-order finite difference scheme for the compressible Navier-Stokes equations, no-slip wall boundary conditions," *Journal of Computational Physics*, Vol. 227, No. 10, May 2008, pp. 4805–4824.

[56] Nordström, J., Gong, J., van der Weide, E., and Svärd, M., "A stable and conservative high order multi-block method for the compressible Navier-Stokes equations," *Journal of Computational Physics*, Vol. 228, No. 24, 2009, pp. 9020–9035.

[57] Kreiss, H. O. and Scherer, G., "Finite element and finite difference methods for hyperbolic partial differential equations," *Mathematical Aspects of Finite Elements in Partial Differential Equations*, edited by C. de Boor, Mathematics Research Center, the University of Wisconsin, Academic Press, 1974.

[58] Strand, B., "Summation by parts for finite difference approximations for d/dx," *Journal of Computational Physics*, Vol. 110, No. 1, 1994, pp. 47–67.

[59] Saad, Y. and Sosonkina, M., "Distributed Schur complement techniques for general sparse linear systems," *SIAM Journal of Scientific Computing*, Vol. 21, No. 4, 1999, pp. 1337–1357.

[60] Hicken, J. E., *Efficient algorithms for future aircraft design: Contributions to aerodynamic shape optimization*, Ph.D. thesis, University of Toronto, Toronto, Ontario, Canada, 2009.

[61] Osusky, L., *A numerical methodology for aerodynamic shape optimization in turbulent flow enabling large geometric variation*, Ph.D. thesis, University of Toronto, Toronto, Ontario, Canada, 2014.

[62] de Sturler, E., "Nested Krylov methods based on GCR," *Journal of Computational and Applied Mathematics*, Vol. 67, 1996, pp. 15–41.

[63] de Sturler, E., "Truncation strategies for optimal Krylov subspace methods," *SIAM Journal on Numerical Analysis*, Vol. 36, No. 3, 1999, pp. 864–889.

[64] Hicken, J. E. and Zingg, D. W., "A simplified and flexible variant of GCROT for solving nonsymmetric linear systems," *SIAM Journal on Scientific Computing*, Vol. 32, No. 3, June 2010, pp. 1672–1694.

[65] Gill, P. E., Murray, W., and Saunders, M. A., "SNOPT: an SQP algorithm for large-scale constrained optimization," *SIAM Journal on Optimization*, Vol. 12, No. 4, 2002, pp. 979–1006.

[66] Zingg, D. W., Nemec, M., and Pulliam, T. H., "A comparative evaluation of genetic and gradient-based algorithms applied to aerodynamic optimization," *European Journal of Computational Mechanics*, Vol. 17, 2008, pp. 103–126.

[67] Chernukhin, O. and Zingg, D. W., "Multimodality and global optimization algorithms for aerodynamic shape optimization," *AIAA Journal*, Vol. 51, No. 6, 2013, pp. 1342–1354.

[68] Zingg, D., Leung, T., Diosady, L., Truong, A., Elias, S., and Nemec, M., "Improvements to a Newton-Krylov algorithm for aerodynamic shape optimization," *43rd AIAA Aerospace Sciences Meeting and Exhibit*, AIAA–2005–4857, Reno, Nevada, 2005.

[69] Vassberg, J. C., Tinoco, E. N., Mani, M., Rider, B., Zickuhr, T., Levy, D. W., Brodersen, O. P., Eisfeld, B., Crippa, S., Wahls, R. A., Morrison, J. H., Mavriplis, D. J., and Murayama, M., "Summary of the Fourth AIAA CFD Drag Prediction Workshop," *28th AIAA Applied Aerodynamics Conference*, AIAA–2010–4547, Chicago, Illinois, United States, June 2010.

[70] Levy, D. W., Laflin, K. R., Tinoco, E. N., Vassberg, J. C., Mani, M., Rider, B., Rumsey, C. L., Wahls, R. A., Morrison, J. H., Brodersen, O. P., Crippa, S., Mavriplis, D. J., and Murayama, M., "Summary of data from the Fifth AIAA CFD Drag Prediction Workshop," *51st AIAA Aerospace Sciences Meeting and Aerospace Exposition*, AIAA–2013–0046, Grapevine, Texas, United States, Jan. 2013.

[71] "ANSYS ICEM CFD Tutorial Manual," Tech. Rep. ANSYS ICEM CFD 14.0, ANSYS, Inc., 2011, http://www.ansys.com.

[72] Reist, T. A. and Zingg, D. W., "Aerodynamically Optimal Regional Aircraft Concepts: Conventional and Blended Wing-Body Designs," *52nd AIAA Aerospace Sciences Meeting*, AIAA-2014-0905, National Harbor, MD, January 2014.